Lawrence Berkeley National Laboratory

Title
Frictional properties of Opalinus Clay: influence of humidity, normal stress and grain size on frictional stability

Permalink
https://escholarship.org/uc/item/3w6458r9

Journal
Geophysical Journal International, 233(1)

ISSN
0956-540X

Authors
Bigaroni, Nico
Scuderi, Marco Maria
Cappa, Frédéric
et al.

Publication Date
2022-11-29

DOI
10.1093/gji/ggac457

Copyright Information

Peer reviewed

Frictional properties of Opalinus Clay: influence of humidity, normal stress and grain size on frictional stability

Nico Bigaroni [1], Marco Maria Scuderi,[1] Frédéric Cappa,[2] Yves Guglielmi,[3] Christophe Nussbaum,[4] Luca Aldega [1], Giacomo Pozzi[5] and Cristiano Collettini[1,5]

[1]*Dipartimento di Scienze della Terra, Sapienza Università di Roma,* 00185 *Rome RM, Italy. E-mail:* nico.bigaroni@uniroma1.it
[2]*Université Côte d'Azur, CNRS, Observatoire de la Côte d'Azur, IRD, Géoazur,* 06560 *Valbonne, France*
[3]*Hydrogeology Department, Lawrence Berkeley National Laboratory, Energy Geosciences Division, Berkeley,* 94720 *CA, USA*
[4]*Federal Office of Topography, Swissotopo, Mont Terri Consortium, St-Ursanne, Switzerland*
[5]*Istituto Nazionale di Geofisica e Vulcanologia, INGV, Roma, Italy*

SUMMARY

The Opalinus Clay (OPA) is a clay-rich formation considered as a potential host rock for radioactive waste repositories and as a caprock for carbon storage in Switzerland. Its very low permeability (10^{-19} to 10^{-21} m^2) makes it a potential sealing horizon, however the presence of faults that may be activated during the lifetime of a repository project can compromise the long-term hydrological confinement, and lead to mechanical instability. Here, we have performed laboratory experiments to test the effect of relative humidity (RH), grain size (g.s.) and normal stress on rate-and-state frictional properties and stability of fault laboratory analogues corresponding to powders of OPA shaly facies. The sifted host rock powders at different grain size fractions (<63 μm and 63 < g.s. < 125 μm), at room (∼25 per cent) and 100 per cent humidity, were slid in double-direct shear configuration, under different normal stresses (5–70 MPa). We observe that peak friction, μ_{peak} and steady-state friction, μ_{ss}, depend on water vapour content and applied normal stress. Increasing relative humidity from ∼25 per cent RH (room humidity) to 100 per cent RH causes a decrease of frictional coefficient from 0.41 to 0.35. The analysis of velocity-steps in the light of rate-and-state friction framework shows that the stability parameter (a–b) is always positive (velocity-strengthening), and it increases with increasing sliding velocity and humidity. The dependence of (a–b) on slip rate is lost as normal stress increases, for each humidity condition. By monitoring the variations of the layer thickness during the velocity steps, we observe that dilation (Δh) is directly proportional to the sliding velocity, decreases with normal stress and is unaffected by humidity. Microstructural analysis shows that most of the deformation is accommodated within B-shear zones, and the increase of normal stress (σ_n) promotes the transition from strain localization and grain size reduction to distributed deformation on a well-developed phyllosilicate network. These results suggest that: (1) the progressive loss of velocity dependence of frictional stability parameter (a–b) at σ_n > 35 MPa is dictated by a transition from localized to distributed deformation and (2) water vapour content does not affect the deformation mechanisms and dilation, whereas it decreases steady-state friction (μ_{ss}), and enhances fault stability.

Key words: Fault zone rheology; Friction; Dynamics and mechanics of faulting; Microstructures; Rheology and friction of fault zones; Opalinus Clay; Geological repositories.

1 INTRODUCTION

The Opalinus Clay (OPA) is a clay-rich formation that is being considered as potential host rock for radioactive waste repositories (Bossart *et al.* 2018) and as a caprock for carbon storage (Zappone *et al.* 2021). To avoid contamination of air and underground water, the goal of a geological repository is to guarantee a permanent confinement and isolation for high-level nuclear waste, as well as for the CO$_2$ injected at depth (Tsang *et al.* 2015). OPA can act as a fluid barrier because of very low permeability (10^{-19} to 10^{-21} m^2; Orellana *et al.* 2019), adsorption properties (clay minerals are well suited to retain radionuclides, Bossart *et al.* 2018), and self-sealing behaviour by swelling capacity of certain clay minerals (Bock *et al.* 2010; Voltolini & Ajo-Franklin 2020).

The hydrogeological, geochemical and geotechnical characterization of OPA is conducted at the Mont Terri Laboratory (MTL), an underground research facility located at about 340 m depth in the northern part of Switzerland (Thury & Bossart 1999; Nussbaum *et al.* 2011). The laboratory is situated within the Opalinus Clay, in the southern limb of the Mont Terri anticline and its tunnels cross-cut a 1.5–3 m thick non-active fault zone namely the 'Main Fault' (Nussbaum *et al.* 2018; Guglielmi *et al.* 2020; Fig. 1a). The fault zone contains a variety of structures such as fractures, calcite veins, undeformed rock, bedding planes, scaly clay and OPA Clay-fault gouge (Nussbaum *et al.* 2011; Bossart *et al.* 2018; Laurich *et al.* 2018; Fig. 1c).

In the context of geological repositories, the presence of faults represents a critical element that has to be taken into account during the site characterization process of a storage formation (Tsang *et al.* 2015). Faults can act as a possible pathway for fluids, favouring the premature loss of CO_2 or radioactive material dissolved in the water in the form of radionuclides, by migrating in the surrounding aquifer, and thus polluting the environment (Wang *et al.* 2001; Tsang *et al.* 2012, 2015). The risk of any damage to the Opalinus Clay formation caused by the mechanical re-activation of faults must be evaluated during the diverse life stages of the geological repository. During the repository construction phases, recent studies highlight how new mining activities can cause mechanical instability on nearby fault zones (Hopp *et al.* 2022). Similar excavation damages can be expected all through the operational and closing phases of underground galleries (Nussbaum *et al.* 2011; Popp *et al.* 2008). In the context of carbon capture and storage (CCS), a potential risk factor is associated with the reactivation of ancient tectonic fault systems during injection operations of large volumes of CO_2 (Rutqvist *et al.* 2016). Therefore, even of modest magnitude, damage due to induced seismicity can compromise the long-term confinement and containment capabilities of the OPA formation (Bossart *et al.* 2018). Thus, understanding the frictional and hydromechanical properties of faults within OPA Clay it is of relevance for geological carbon storage and nuclear waste disposal.

Previous laboratory studies have focused on exploring how scaly clays and the clay-fault gouge control the mechanical behaviour of the faults within the OPA formation and therefore also of the 'Main Fault' (Fang *et al.* 2017, 2018; Orellana *et al.* 2018a, 2018b, 2019). Laboratory friction experiments at subsurface conditions and subseismic slip velocities showed that scaly clays have either velocity strengthening or velocity weakening behaviour that might have the potential to control and nucleate seismicity within the OPA formation (Orellana *et al.* 2018a). The OPA Clay-fault gouge, however, shows a velocity strengthening behaviour that would favour aseismic slip, resulting in stable fault creeping over geological timescales (Fang *et al.* 2017, 2018; Orellana *et al.* 2018b). Recently, Orellana *et al.* (2019) observed that, under laboratory conditions of controlled water saturation (dry and wet), low effective normal stresses and subseismic velocities, OPA Clay-fault gouge upon velocity downstep has the tendency of shear-enhanced compaction coupled with a decrease in permeability (similar observations in other materials by Zhang & Cox 2000; Segall *et al.* 2010; Scuderi *et al.* 2017a; Im *et al.* 2018).

Decametric scale in-situ fluid injection experiments performed directly within the 'Main Fault' structure were able to reactivate the 'Main Fault' with small displacement (i.e. from tens to about a hundred of microns) and associated seismic events (Guglielmi *et al.* 2020; Jeanne *et al.* 2018; Cappa *et al.* 2022). During these *in situ* experiments, by measuring the pressure of the fluids and displacement signals directly from the fault, it was possible for the Authors to estimate the evolution of fault-parallel displacement (i.e. slip) and fault perpendicular displacement (i.e. dilation) and to measure how the fault permeability evolved as a function of time and pressure increase (Guglielmi *et al.* 2020). Similar results have been observed from laboratory experiments aimed at replicating fault reactivation by fluid injection at similar boundary conditions of the MTL, in shale-bearing (Scuderi & Collettini 2018) and limestone fault gouges (Cappa *et al.* 2019). Taken together these recent experiments (both *in situ* and in the laboratory) show that, after the reactivation by fluid injection of a critically stressed fault (sensu Walsh & Zoback 2016), the slip starts as an accelerating aseismic creep coupled with fault dilation. As the slip and fluid injection continue further, the frictional sliding is mainly controlled by a rate strengthening behaviour that promotes stable aseismic slip.

In this paper, we present a comprehensive study of the rate-and-state frictional properties of OPA Clay-fault powder considered a gouge analogue, over a wide range of normal stress (5–70 MPa), grain size ($<63~\mu$m and $63 < $ g.s. $< 125~\mu$m) and relative humidity conditions ($\sim$25 per cent). Our main goal is to improve our understanding on how these variables influence fault strength and frictional stability upon reactivation of OPA Clay. The influence of grain size and applied normal stress above 30 MPa on the OPA Clay friction are experimental conditions that have not been tested previously, as well as the quantification of dilation following velocity up-steps. We expand the boundary conditions of normal stresses above those expected to occur at typical depths of geologic repositories, to obtain a more comprehensive view of OPA Clay frictional properties. Thus, our results could also generate a benchmark for studies applied to CO_2 sequestration in deep reservoirs, caprocks integrity and seismic behaviour of decollement zones. To obtain the OPA Clay friction properties, we performed velocity step sequences and slide-hold-slide (SHS) tests in a double direct shear configuration, monitoring the evolution of layer thickness as a proxy for the volumetric deformation of the gouge layers. Finally, we discuss our results under the light of microstructural observations (i.e. SEM analysis), to develop a conceptual model that couples the deformation mechanisms and the mechanical data.

2 MATERIALS AND METHODS

2.1 Experimental samples

To study the frictional properties of the Opalinus Clay gouge, we sheared pulverized samples of undeformed OPA Clay retrieved from the monitoring drill core BFS-1 (0.14 m in diameter; Guglielmi *et al.* 2020) 37.40 m below the MTL galleries, just outside the 'Main Fault' zone, in the host rock (Fig. 1).

We prepared the gouge samples by crushing the undeformed OPA sample (Fig. 1c) with a ball mill for less than two seconds to avoid any thermal damage to the mineral grains due to the heat generated by friction during milling spin. To understand the influence of grain size (g.s.), the powdered sample was subdivided into two batches at different grain sizes, a coarser one sieved between 63 and 125 μm and the finer one having g.s. $<63~\mu$m.

The mineralogical assemblage was determined by XRD analysis on the same powders used for the friction experiments (g.s. $<63~\mu$m and $63 < $ g.s. $< 125~\mu$m). The analysis was conducted using a Bruker D8 Advance X-ray system equipped with Lynxeye XE-T silicon-strip detector at the Department of Earth Sciences, Sapienza University of Rome (Italy). The instrument was operated at 40 kV and 30 mA using CuKα radiation ($\lambda = 1.5406$ Å). Samples were run
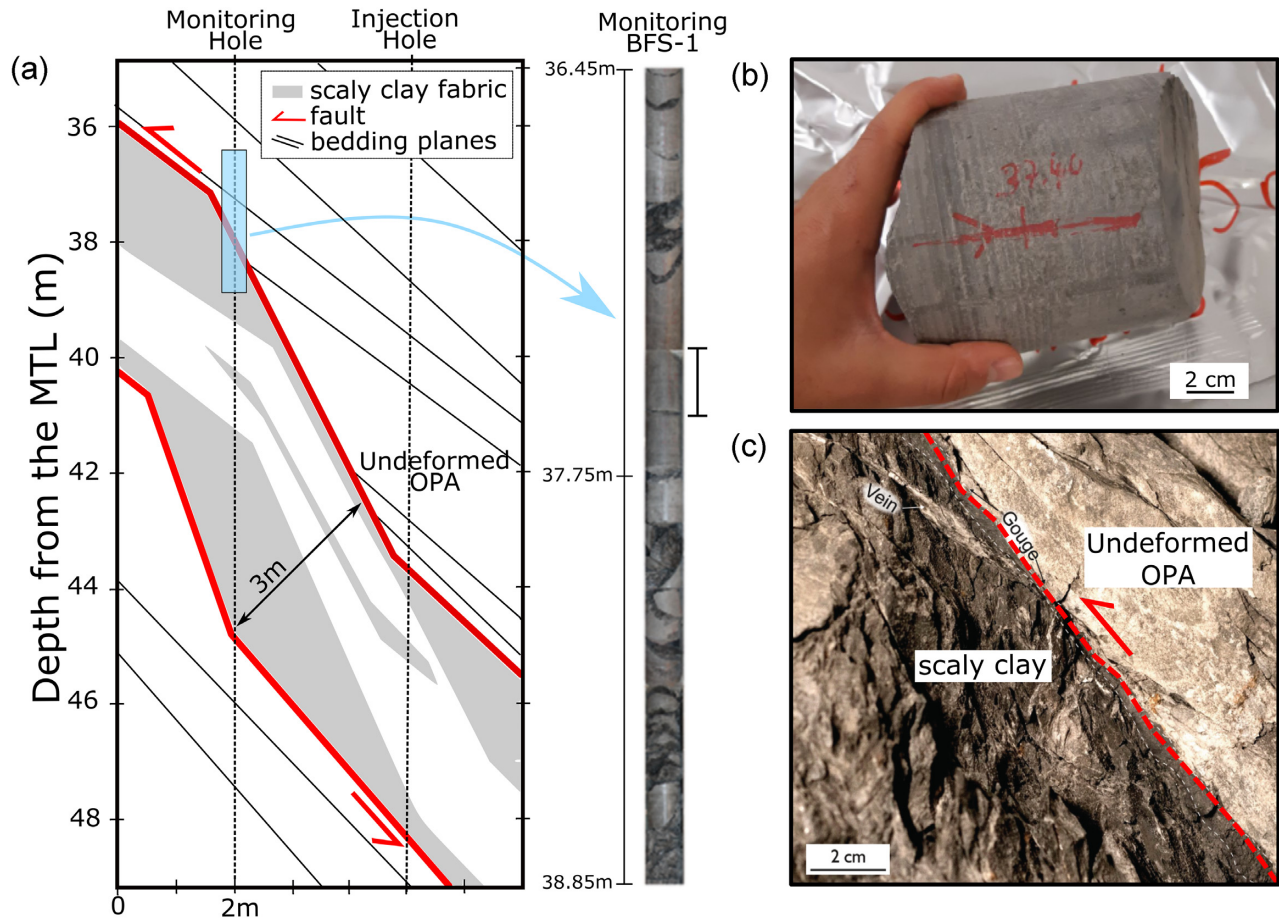
Figure 1. (a) Vertical cross-section showing the 'Main Fault' (bounded in red) at Mont Terri Laboratory (MTL). The grey patches are the scaly clay fabric within the 'Main Fault. The blue rectangle shows the location of the optical log of BFS-1 (modified from Guglielmi *et al.* 2020). The black bar on the core log shows the exact location where the core sample of intact host rock of OPA was retrieved. (b) Detail of the core rock sample used during lab experiments. (c) Outcrop picture of the shear zone at the top 'Main Fault' surface in tunnel 98, where the gouge appears as thin discontinuous lenses between scaly clay and undeformed OPA (modified from Laurich *et al.* 2018).

between 2° and 70° 2θ with step sizes of 0.02° 2θ while spinning the sample. Data were collected with variable slit mode to keep the irradiated area on the sample surface constant and converted to fixed slit mode for semiquantitative analysis. Semiquantitative estimation of mineral phases was performed by calculating peak areas and using mineral intensity factors as calibration constants (Moore & Reynolds 1997).

X-ray semiquantitative analysis (Table 1) shows that the OPA Clay gouges are mainly made up of sheet silicates (55–58 per cent) including kaolinite, chlorite, illite/muscovite and mixed layers illite-smectite, calcite (21–22 per cent), quartz (14–15 per cent) and pyrite (4 per cent) without substantial difference in mineral content between the two grain size fractions tested. K-feldspar, albite and ankerite do not exceed 2 per cent. Such mineralogical composition and weight per cent of mineral phases is consistent with the results shown by Klinkenberg *et al.* (2009) and Fang *et al.* (2017).

2.2 Experimental procedure

We performed experiments using a biaxial, versatile, rock deformation apparatus (BRAVA, Collettini *et al.* 2014; Fig. 2a). The apparatus was used in the double- direct shear configuration which consists of two layers of powdered gouge samples sandwiched in

a three-steel block assembly (Fig. 2b). This configuration is characterized by two stationary side blocks and a sliding central block with a nominal frictional contact area of 50 mm × 50 mm. During the assembly preparation, for all the experiments, each layer has been constructed maintaining a constant initial thickness of 5 mm.

To explore the influence of relative humidity (RH) conditions on the frictional behaviour of the OPA Clay we prepared samples at 100 per cent RH, and at room humidity. We monitored the water vapour content with a hygrometer during each experimental phase. For the experiments at room humidity, we measured values between ∼20 and ∼30 per cent RH so, from here on, we refer to ∼25 per cent RH as an intermediate value for room humidity experiments. For each of the 100 per cent relative humidity experiments, we prepared the sample assembly (i.e. forcing blocks plus gouge) the day before and left overnight in a controlled humid environment for 24 hr (humidifier cell). The humidity of the environment was logged using a hygrometer and ensured that was maintained at 100 per cent. To evaluate the amount of humidity prior to the experiment we measured a ∼15 per cent weight increase during the overnight humidification procedure, that is a reasonable value for adsorbed water under a 100 per cent humid environment (e.g. Morrow *et al.* 2017). To avoid dehydration of swelling minerals, samples were constructed fast (it usually takes about 5 min for this configuration) and immediately placed in the apparatus vessel. We conducted the

Table 1. XRD data for the simulated gouges derived from core samples of monitoring hole (BFS-1) at 37.40 m of depth from the Mont Terri Laboratory (MTL) in Switzerland.

Grain-size (µm)	Bulk mineral composition (wt. per cent)						
	Ph	Qz	Cal	Py	Ab	Kfs	Ank
g.s. < 63	58 per cent	14 per cent	21 per cent	4 per cent	1 per cent	1 per cent	1 per cent
63 < g.s. < 125	55 per cent	15 per cent	22 per cent	4 per cent	2 per cent	1 per cent	1 per cent

Note: Ph-phyllosilicate minerals (kaolinite, chlorite, illite/muscovite, mixed layers illite-smectite), Qz-quartz, Cal-calcite, Py-pyrite, Ab-albite, Kfs- k-feldspar, Ank-Ankerite.
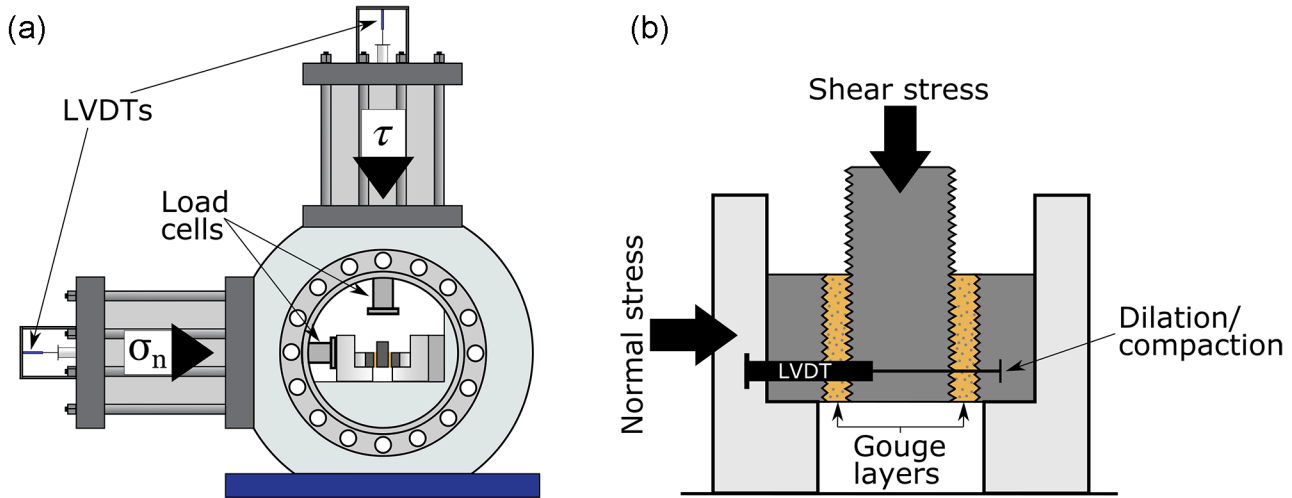
Figure 2. (a) Sketch of the Rock Deformation Apparatus BRAVA at INGV of Rome (not in scale). (b) Schematics of the assembly. Normal stress and Shear stress are applied by two different hydraulic rams. The dilation (Δh) and compaction are measured using an on board LVDT.

whole experiment with the humidifier inside the vessel, closed on both sides by plexiglass panels to ensure 100 per cent humidity. All experiments were run at room temperature (∼25 °C).

The experimental dataset was designed also to study the influence of the grain size on frictional properties. For this reason, for each experimental condition (of normal stress and relative humidity) we carried out two experiments, one with an initial grain size <63 µm and the other with grain size between 63 and 125 µm (for more details see Table S1).

The deformation apparatus BRAVA uses two servo-controlled hydraulic rams to apply the horizontal and vertical loads (Collettini *et al.* 2014). The applied load (both horizontal and vertical) was measured via strain gauge load cells (accuracy ±0.03 kN) positioned at the extremity of the hydraulic rams in contact with the sample assembly. To measure the horizontal and vertical displacements we used two linear variable displacement transformers (LVDT), one for each ram, with an accuracy of ±0.1 µm. We corrected for the stretch of the vertical frame with a value of 0.116801 MPa µm⁻¹ when the shear stress is <10 MPa, and with 0.30146 MPa µm⁻¹ when it is >10 MPa. To account for the stretch of the horizontal frame we corrected with a value of 0.12536 MPa µm⁻¹ when the normal stress is <20 MPa, and with 0.41656 MPa µm⁻¹ when it is >20 MPa. At any time of the experiment, as needed, the two pistons can be controlled either through a load feedback control mode, to maintain a constant load, or a displacement feedback control mode, to apply a constant displacement rate.

At the beginning of each experiment, we advanced the horizontal piston in displacement control at velocity of 1 µm s⁻¹, up to 1 kN of horizontal load. We then switched the control feedback in load control mode, increasing the horizontal load stepwise by 1 kN every minute. Once we reached the target value, we waited 30 min to allow the two gouge layers to compact to a steady-state,

constantly monitoring the total thickness using the horizontal LVDT (Fig. 2b). We start shearing the sample by advancing the vertical ram in displacement control at a constant velocity of 10 µm s⁻¹ until steady-state sliding. Initially, the sample deformed quasi-elastically up to a peak friction value (blue square in Fig. 3) followed by a frictional evolution to a steady-state sliding frictional strength (blue circle in Fig. 3). To study the velocity dependence of friction and infer frictional stability with accumulated shear strain, we performed two sets of velocity step tests where we changed the shear velocity quasi-instantaneously stepwise from 1 to 300 µm s⁻¹ with a three-fold increase. The velocity step series were separated by a series of slide-hold-slides (SHS), with hold time ranging from 1 to 3000 s that we use to calculate frictional healing. This range of tested values is motivated by previous studies that showed this experimental protocol is well adapted for the estimation of frictional properties of gouge materials (e.g. Marone 1998).

To estimate the frictional properties and fault slip stability, the rate-and-state (R&S) friction framework was used (Dieterich 1979; Marone 1998; Scholz 1998). These constitutive law describes the evolution of the coefficient of friction (μ) in terms of a constant initial friction (μ_0) suitable for steady-state slip at a reference velocity (V_0), a term that describes the direct effect a and a term to express the evolution effect b, over a critical distance D_c and an evolving state parameter θ, that can be interpreted as the average life-time of contacts (Dieterich 1979; Ruina 1983; Marone 1998):

$$\mu = \mu_0 + a \ln\left(\frac{V}{V_0}\right) + b \ln\left(\frac{V_0\theta}{D_c}\right). \qquad (1)$$

The evolution law for the state variable θ is given by:

$$\frac{d\theta}{dt} = -\frac{V_0}{D_c} ln\left(\frac{V\theta}{D_c}\right). \qquad (2)$$
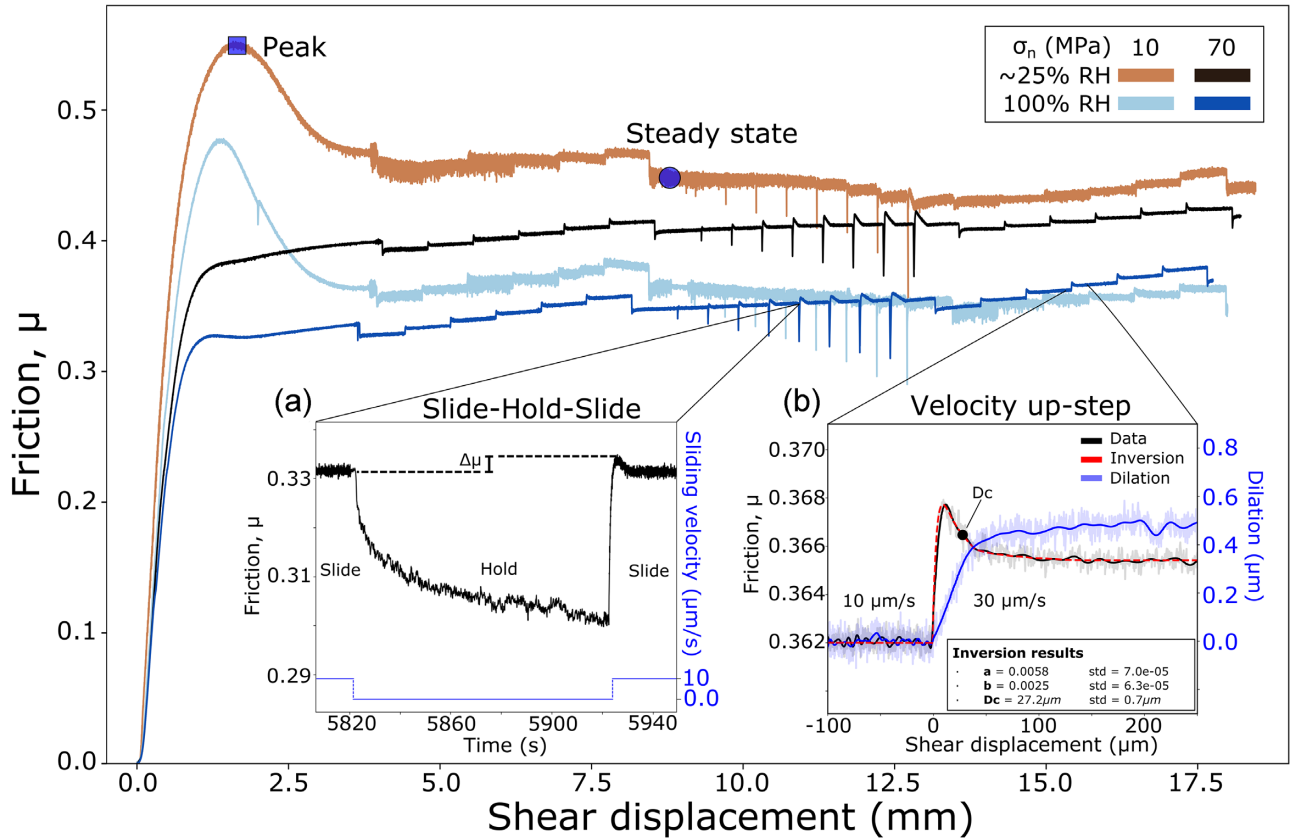
Figure 3. Representative frictional experiments sheared at high (70 MPa) and low (10 MPa) normal stress, under different relative humidity (RH) conditions. The blue square inside the 'run-in' phase (0–4 mm) and the blue circle, are the points where in all the experiments were taken respectively peak and steady-state friction. (a) Example of slide-hold-slide test in time. (b) Example of one velocity step where the best fit of the inversion model (in red) over the experimental data (in black) is plotted with fault dilation (in blue). Inversion results with standard deviations are reported in the box.

Eq. (1) coupled with eq. (2) is usually referred to as the Ruina or slip law. The choice of this evolution law is motivated by recent studies showing a good fit to experimental frictional data (Bhattacharya *et al.* 2017; Scuderi & Collettini 2018). The steady-state velocity dependence of friction is described by the constitutive parameter $(a–b)$ (eq. 3):

$$a - b = \frac{\Delta \mu_{ss}}{\ln \left(\frac{V}{V_0} \right)} , \tag{3}$$

where $\Delta \mu_{ss}$ is the change in the steady-state friction upon an immediate change in sliding velocity from V_0 to V (Marone 1998). If friction increases with increasing velocity, $(a–b) > 0$, the material is velocity strengthening and slip is inherently stable, leading to aseismic fault creep (Fig. 3b). However, if the material is velocity weakening, $(a–b) < 0$, frictional strength decreases with slip velocity and slip may be unstable, and any perturbation on the fault can potentially promote slip acceleration. We modelled our laboratory frictional data using an iterative least square loop based on a fifth order Runge–Kutta method (Reinen & Weeks 1993; Saffer & Marone 2003). The results of the iterations for each velocity step allow us to determine the best fit parameters of the velocity step test, that is the critical slip distance D_c, the parameters a and b, and their respective variances.

The amount of frictional healing, $\Delta \mu$, was measured as the difference between the peak friction measured upon reshear after each hold and the post-hold steady-state friction (Marone 1998; Fig. 3a).

Frictional healing rates β were calculated as:

$$\beta = \frac{\Delta \mu}{\Delta (t_h)} . \tag{4}$$

Volumetric changes in the simulated fault gouge during deformation are evaluated by analysing the evolution of the layer thickness of the fault gouge deforming at constant frictional contact area. During the experiments gouge layers undergo continuous bulk compaction due to material loss related to the geometry of the DDS configuration (e.g. Scott *et al.* 1994; for more details see the evolution of the layer thickness during shear sliding, Fig. S2). We calculate the amount of dilation (Δh) during velocity steps (Fig. 3b) by removing the bulk compaction trend in layer thickness by using a least square fit to the data in an interval following the transient phase of velocity steps, that is after D_c (for more details see Fig. S3), as outlined by Samuelson *et al.* (2009) (see also Marone *et al.* 1990; Mair & Marone 1999; Scuderi *et al.* 2017b; Giacomel *et al.* 2021).

2.3 Microstructural analysis

To obtain information on the deformation mechanisms that modulate slip behaviour of OPA, we performed microstructural analyses using a scanning electron microscope (SEM). After selected experiments we collected the gouge material of the post-mortem samples, carefully detaching it from the steel forcing blocks using a copper foil (0.8 mm thick), and then impregnated with two components epoxy resin. Once the resin had hardened, the samples were smoothed in dry conditions with sandpaper up to 5000 grit
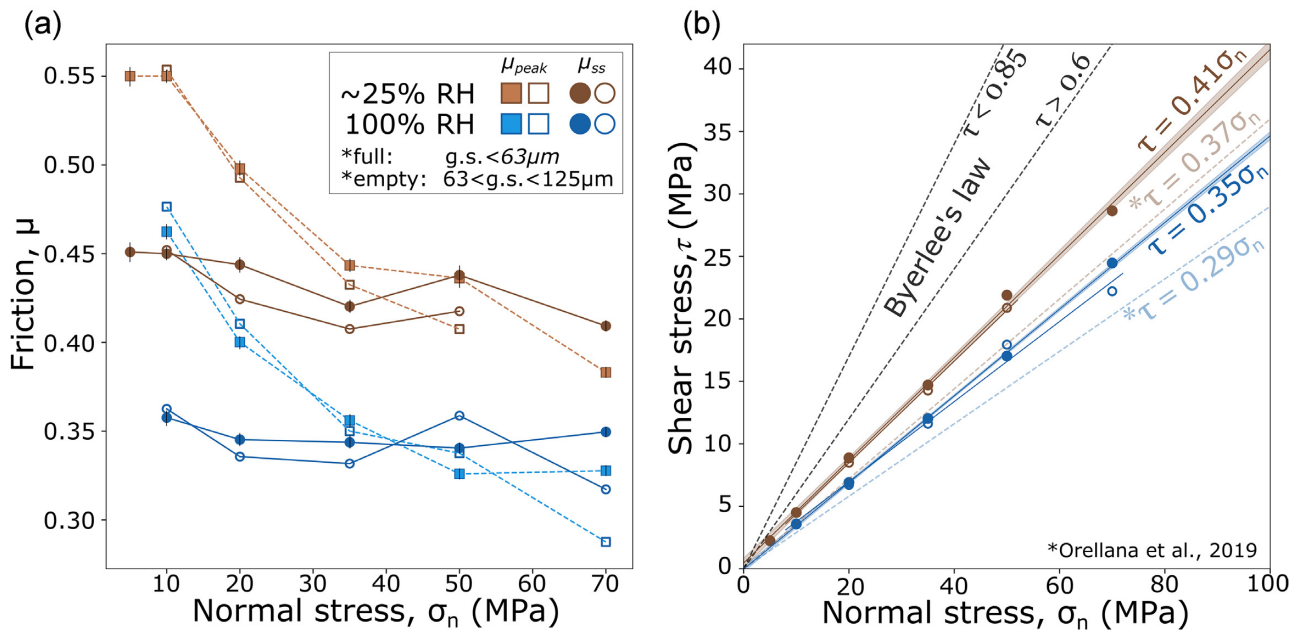
Figure 4. (a) Evolution of friction (μ) as a function of normal stress. Squares and circles represent, respectively, the μ_{peak} and the μ_{ss}. Brown is for room humidity (RH) experiments; blue is for the 100 per cent RH ones (light for μ_{peak} and dark for μ_{ss}). Empty symbols are experiments at higher initial grain size ($63 < g.s. < 125\ \mu m$); full symbols are g.s. $< 63\ \mu m$. (b) Shear strength in a Mohr-Coulomb space. Frictional coefficient of OPA Clay is the slope of the linear best fit for τ_{ss} values (brown for room humid; blue for 100 per cent RH), with the shaded area that corresponds to $\pm 1\sigma$. For comparison, we have included Byerlee's law and previous results of frictional experiments carried out under dry and 100 per cent humidity conditions on OPA Clay gouges by Orellana *et al.* (2018b, 2019).

and coated with graphite. The samples thus prepared, were then analysed with a scanning electron microscopy (SEM), model FEI Quanta 400, using backscattered diffraction (BSD) images.

3 RESULTS

3.1 Frictional strength

The typical experimental curves that we observe in response to the application of shear deformation usually show a peak in shear strength (μ_{peak}) that is followed by a strain weakening stage until the achievement of a steady-state shear strength (μ_{ss}; Fig. 3; e.g. Samuelson & Spiers 2012; Den Hartog & Spiers 2013; Haines *et al.* 2013; Kohli & Zoback 2013). The value of steady-state friction (blue dot in Fig. 3) was taken just before the first hold of the slide-hold-slide (SHS) test. This is because, after the first cycle of velocity-steps (at ~9 mm of displacement and velocity of 10 $\mu m\ s^{-1}$), almost all experiments show a steady-stable sliding, which does not always occur after the peak friction and subsequent strain weakening (at the end of the 'run-in' phase). In Fig. 4 we show the evolution of peak (μ_{peak}) and steady-state (μ_{ss}) friction as a function of normal stress (σ_n). We observe that μ_{peak} is normal stress dependent and decreases as the normal stress (σ_n) increases for all the boundary conditions of room humidity and grain size (Fig. 4a). Differently, μ_{ss} is weakly normal stress dependent and is constant for all the boundary conditions.

The major variation in frictional strength is related to the presence of water (i.e. relative humidity) in our sample, causing a systematic reduction in friction. Room humidity experiments show values between ~0.38 and ~0.55 for μ_{peak} and ~0.42 to ~0.45 for μ_{ss}. However, in experiments conducted at 100 per cent RH, μ_{peak} varies between ~0.30 and ~0.46, whereas μ_{ss} is almost constant at ~0.35.

The fault gouge with g.s. $< 63\ \mu m$ (Fig. 4a), shows an average reduction of ~19 per cent in μ_{peak} and of ~22 per cent in μ_{ss}, with the increase in relative humidity. The experiments with gouge grain size $63 < g.s. < 125\ \mu m$, displayed an average reduction due to RH increase of 17 per cent for μ_{peak} and 18 per cent, for μ_{ss}. The friction coefficient calculated in a Mohr–Coulomb space (Fig. 4b) using a linear fit of the shear stress values at steady-state (τ_{ss}), is 0.41 $\pm$ 0.01 for room humidity experiments and 0.35 $\pm$ 0.01 for 100 per cent humidity.

3.2 Velocity dependence of friction

The results obtained from the modelling of velocity step experiments are summarized in Fig. 5. This figure shows the evolution of the stability parameter ($a-b$) as a function of the sliding velocity and applied normal stress for room humidity (Fig. 5a) and for 100 per cent RH (Fig. 5b) experiments (see also Table S1 and Fig. S5).

For all the experiments and investigated boundary conditions, the stability parameter ($a-b$) shows a velocity strengthening behaviour ($a-b > 0$) suggesting stable aseismic creep (Fig. 5). In general, our results show that the increase in RH and normal stress has a major influence on controlling fault stability, while the starting grain size has little to no influence. Under room humidity conditions and low normal stress, the evolution of ($a-b$) is strongly controlled by the shear velocity, starting from near velocity neutral values at low velocity ($< 10\ \mu m\ s^{-1}$) and increasing to marked velocity strengthening at the highest velocities ($> 30\ \mu m\ s^{-1}$; Fig. 5a). As the normal stress increases the dependence of ($a-b$) on the sliding velocity vanishes with values that stabilize around 0.002. Adding water causes an overall increase of the ($a-b$) values toward the velocity strengthening field when compared to the room humidity experiments (Fig. 5b). As it was observed under room humid
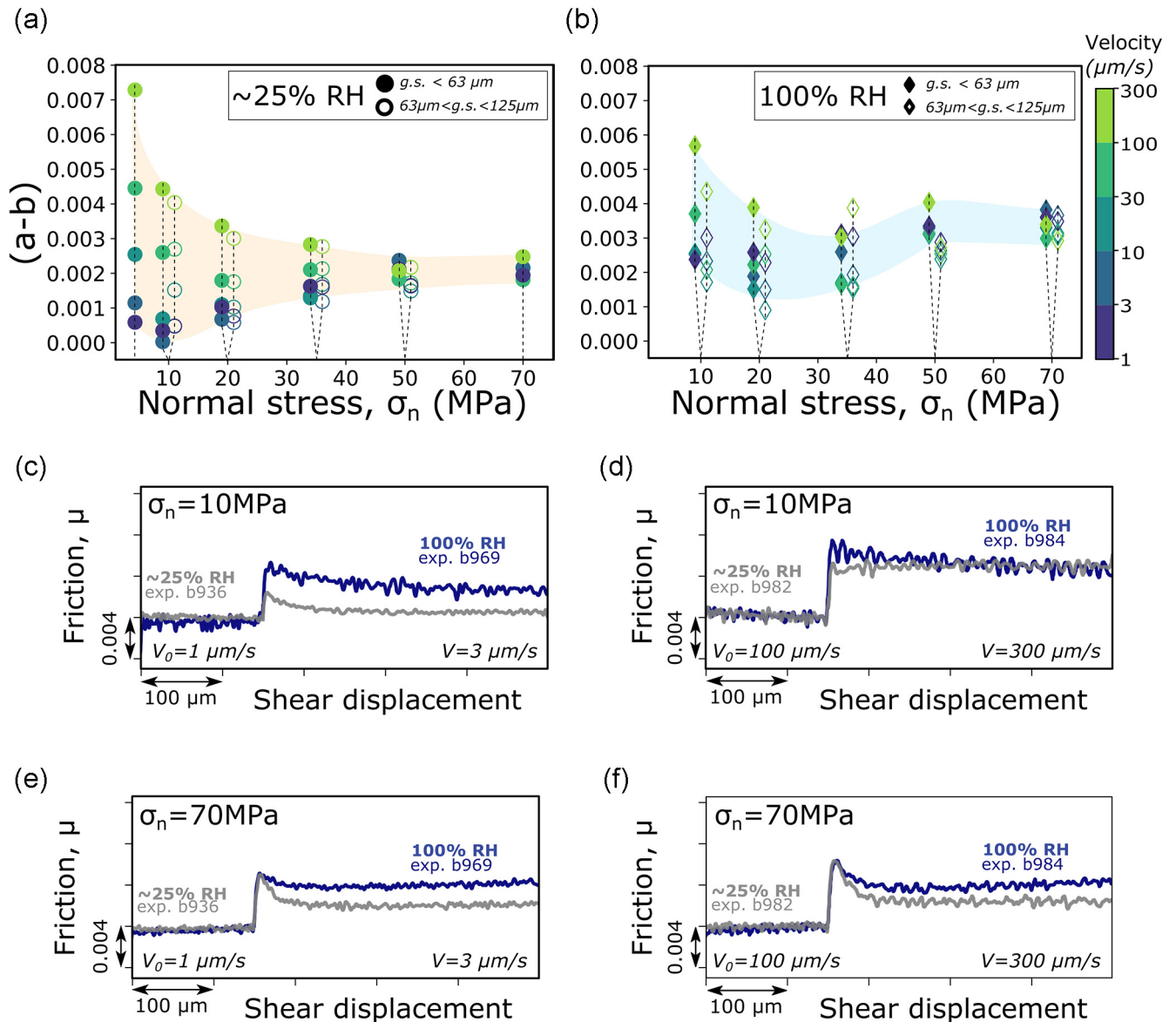
Figure 5. Evolution of RSF constitutive parameters (*a*–*b*) with normal stress and velocity (see the colourmap), under (a) room humidity and (b) 100 per cent RH conditions. Full and empty symbols show respectively data from initial grain size <63 μm, and 63 < g.s. < 125 μm. (c) Detail of the frictional response at low normal stress (10 MPa) between room humid (grey) and 100 per cent RH (blue) for velocity up-steps of 1–3 μm s^{-1} and (d) 100–300 μm s^{-1}. (e) Detail of the frictional response at high normal stress (70 MPa) between room humidity (grey) and 100 per cent RH (blue) for velocity up-steps of 1–3 μm s^{-1} and (f) 100–300 μm s^{-1}.

conditions (*a*–*b*) shows a strong dependence on shear velocity (μm s^{-1}) at normal stress <35 MPa, evolving towards velocity independent constant values of ∼0.0035 at normal stress >35 MPa.

The experimental curves show that, at low normal stress (10 MPa), the frictional response following a velocity up-step, of 1–3 μm s^{-1} (Fig. 5c) and 100–300 μm s^{-1} (Fig. 5d), differs significantly with increasing RH. We observe an increase in the direct effect (i.e. the parameter *a* in RSF laws), especially at low slip velocities (Fig. 5c). This behaviour is at the origin of the high values of (*a*–*b*) that we report at low normal stresses. In contrast, for high normal stress (70 MPa) the friction curves do not significantly differ between a velocity up-step of 1–3 μm s^{-1} (Fig. 5e) and 100–300 μm s^{-1} (Fig. 5f), both for room humidity and 100 per cent RH conditions.

For each velocity step we have also calculated fault dilation (Δh) as a proxy of volumetric strain changes (e.g. Marone *et al.* 1990;

Marone & Kilgore 1993; Samuelson *et al.* 2009). Like the evolution of the stability parameter (*a*–*b*), the amount of dilation increases with sliding velocity at low values of normal stress, under room humidity and 100 per cent RH conditions (Figs 6a and b, respectively). As the normal stress increases, the absolute values of dilation decrease and become less dependent on shear velocity. The dilation data for the experiments conducted with an initial grain size of 63 < g.s. < 125 μm (empty symbols in Fig. 6), show values similar to those observed for the g.s. <63 μm, following the same inverse relationship with normal stress.

3.3 Frictional healing

To evaluate the potential for fault restrengthening during quasi-stationary contact we quantify the amount of frictional healing ($\Delta\mu$)
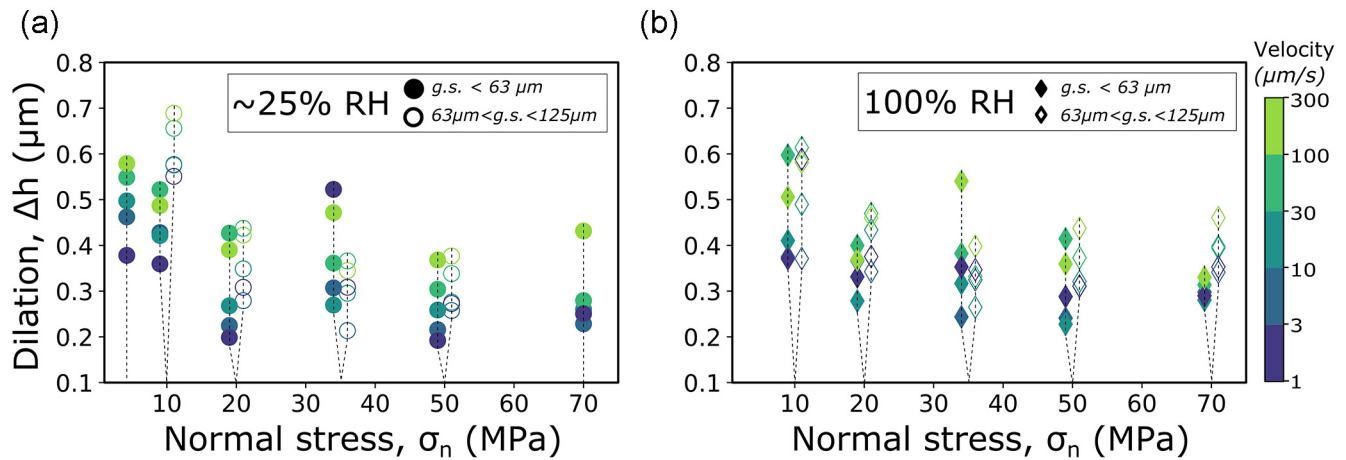
Figure 6. Evolution of dilation (Δh) as a function of normal stress and up-step velocity, both for the (a) room and (b) 100 per cent RH experiments. Full and empty symbols show respectively data from initial grain size <63 μm, and 63 < g.s. < 125 μm.

as a function of hold time (t_h; Fig. 7) to calculate the frictional healing rate (Fig. 8). Our data show that frictional healing is mainly controlled by the hold time and applied normal stress, and subordinately by the presence of water and grain size (Fig. 7). For all the boundary conditions, $\Delta\mu$ increases linearly with the logarithm of hold time and normal stress (see the colour bar in Fig. 7). The presence of water affects the increase in $\Delta\mu$ with normal stress, at any hold time. Experiments conducted at room humidity (Figs 7a and d) show that at low normal stress, the frictional healing has a weak dependence on hold time. As the normal stress is increased above 20 MPa fault strengthening increases with the hold time showing a positive relation with the applied normal stress. Under 100 per cent RH, frictional strengthening always increases as a function of hold time at all normal stresses. This implies that the major differences due to the increase in water vapour content are observed at high hold times. At g.s. <63 μm and hold time of 3000 s, an increase in normal stress from 10 to 70 MPa, results in an increase of $\Delta\mu$ from ~0.0007 to ~0.0098 at room humidity (Fig. 7a), and from ~0.0027 to ~0.0056 at 100 per cent RH (Fig. 7b). For experiments at 63 < g.s. < 125 μm (second row in Fig. 7), the evolution of $\Delta\mu$ with normal stress and hold time is similar to that observed for the smaller grain size. With the bigger grain size, for room humidity experiments (Fig. 7c), as the normal stress increases above 20 MPa, the amount of $\Delta\mu$ is lower than the values measured at lower grain size. Instead, for the experiments at 100 per cent RH we measured similar $\Delta\mu$ values for both the grain sizes.

We performed a best log-linear fit of the frictional healing values to retrieve the frictional healing rate (β). Under any humidity conditions and grain size, we observe a systematic increase of healing rate with normal stress (Fig. 8). For the experiments at g.s. < 63 μm, the addition of water causes the healing rate to decrease at any normal stress values, with the only outlier at 10 MPa. Under these conditions, the largest differences in the frictional healing rate are observed at the highest normal stress (70 MPa), where (β) drops from 0.0025 at room humidity, to 0.0014 at 100 per cent RH conditions. The influence of grain size differs depending on the humidity condition. At 100 per cent RH conditions we observe similar (β) values at any grain size tested (blue curves in Fig. 8). At room humidity conditions, as the normal stress increases above 20 MPa, we observe lower (β) values at 63 < g.s. < 125 μm, compared with experiments at smaller grain size (brown curves in Fig. 8).

3.4 Microstructural analysis

To couple the frictional behaviour with the details of strain accommodation as a function of normal stress, humidity, and grain size, we analyze SEM images of postmortem samples. The analysis of the strain accommodation mechanisms (i.e. localized or distributed) is based on the geometric relationship described by Logan *et al.* (1992) for granular fault gouges (see also: Tchalenko 1970; Marone *et al.* 1992). In detail, we use the term B-shear to describe a continuous shear band, parallel to the slip direction, located at the contact with the indentation of the lateral forcing steel blocks, often found in both sides of the gouge layer. With R-shears we identify shear bands that fully or partially cross, at a low angle, the bulk gouge volume. Both B- and R-shears are characterized with variable degree of grain-size reduction and localization. Within these shear zones we recognize a S-C type fabric, characterized by S-shaped foliation tilted toward the shear direction, and bounded by a continuous alignment of platy minerals, parallel to slip direction (C-planes). With P-like foliation we identify alignments of anisotropic grain, starting from the B-shears, that penetrate the bulk volume of the gouge with opposite inclination to the R-shears (Tchalenko 1970; Passchier & Trouw 2005).

At low-normal stress of 10 MPa (Fig. 9), most of the deformation is accommodated within tens of microns thick B-shears, either under room humidity (Fig. 9e) or 100 per cent RH conditions (Fig. 9f). These B-shears are parallel to the slip direction and are characterized by grain size reduction and misaligned sheet silicates that surround bigger clasts (Figs 9e and f). In the bulk volume of the gouge, we report the presence of OPA Clay aggregates (i.e. microliths, Laurich *et al.* 2017) distributed in a matrix composed of sheet silicates, quartz, and calcite grains (Figs 9b and d). The OPA Clay aggregates have heterogeneous grain size, typically between 20 and 60 μm, and are constituted by undeformed vestigial OPA minerals assemblage, that indicate little deformation in the bulk (see also Fig. S4 in Supporting Information). Increasing humidity has little influence on how deformation is accommodated, being characterized by localized cataclasis and grain size reduction within the B-shears (Figs 9c and d). Compared to the samples at room humidity we observe two B-shears (Fig. 9c), characterized by grain size reduction combined with development of incipient S-C type fabric (Figs 9d and f). Starting from the edges of the sample structure, we report the presence of incipient R-shears, which start from the
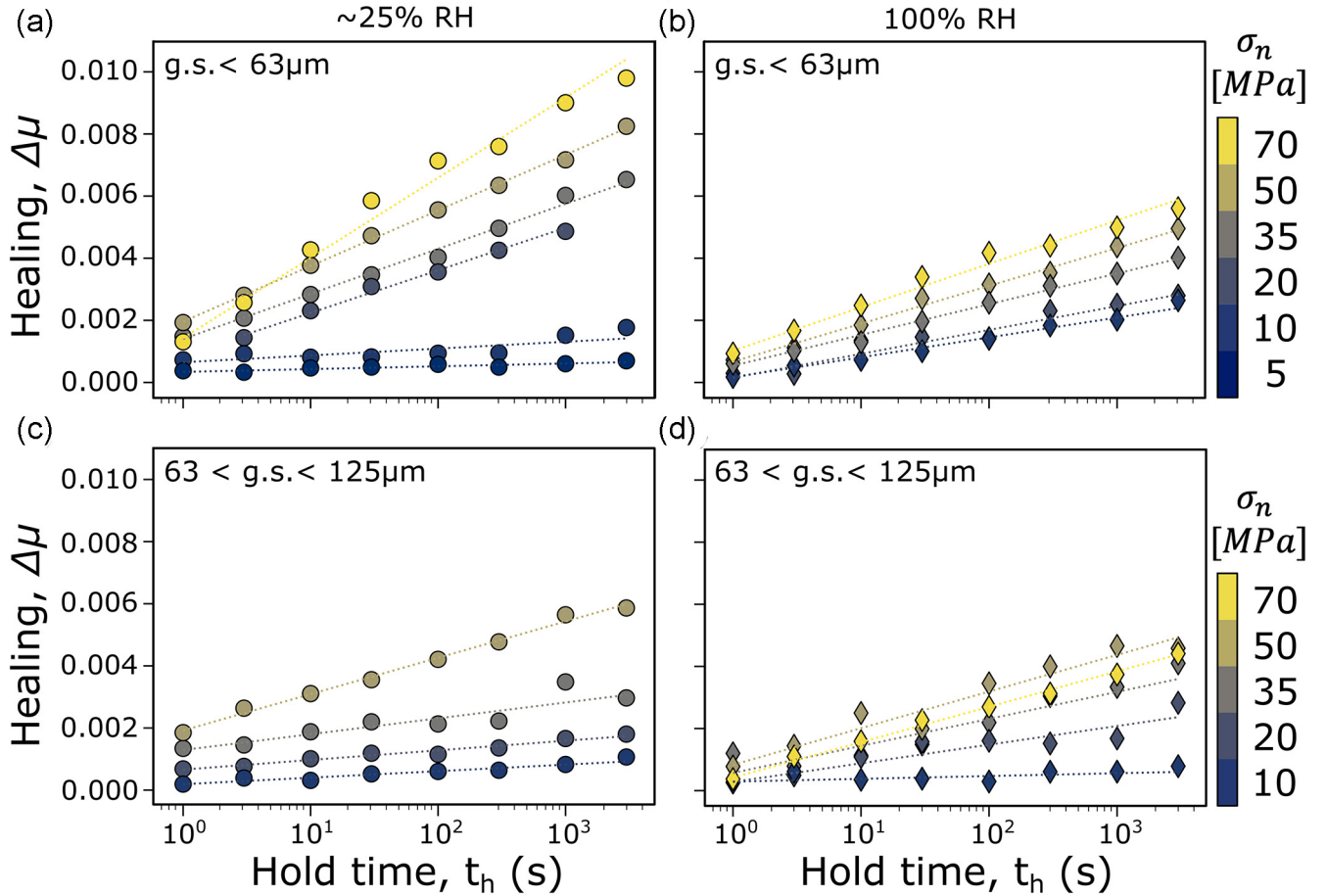
Figure 7. Evolution of the frictional healing $\Delta\mu$ as a function of hold time (t_h) and normal stress (see the colormap). In the first row we plot the evolution of $\Delta\mu$ with t_h for the experiments at g.s < 63 μm, under (a) room humidity and (b) 100 per cent RH conditions. In the second row we plot the corresponding $\Delta\mu$ values for the experiments at 63 < g.s < 125 μm, under (c) room humidity and (d) 100 per cent RH conditions.

B-shears at low angle (∼25°) and fade out within the bulk losing their continuity (Fig. 9c).

At high normal stress (70 MPa, Fig. 10) the deformation is distributed throughout the bulk volume via incipient P-like foliation and low angle R-shears (Figs 10a and b), as also supported by the total absence of OPA Clay aggregates. The P-like foliation and R-shears are high shear-strain zones, characterized by grain size reduction combined with the development of S-C fabric (Figs 10b and d). The P-like foliation forms an angle of approximately 45° with the B-shears and is marked by the alignment of pyrite framboids (Fig. 10e) or elongated calcite grains (Fig. 10f). In experiments conducted at low normal stress, the increase of water vapor content does not change the overall texture of the microstructures (Figs 10c and d). Looking closely, we can only see small variations in fabric, with C-planes of the S-C type fabric, better organized and continuous in 100 per cent RH conditions (Fig. 10f) than in room humidity conditions (Fig. 10d).

4 DISCUSSION

4.1 The origin of frictional strength and water induced weakening

The frictional strength of OPA measured in our laboratory experiments is generally low, ranging between $0.35 < \mu_{ss} < 0.45$, when compared with the classic view proposed by Byerlee's results (i.e. $0.6 < \mu_{ss} < 0.8$; Byerlee 1978) and is consistent with previous results on the same material (Orellana *et al.* 2018b, 2019) and mixtures of clay and granular materials (e.g. Bos *et al.* 2000; Ikari *et al.* 2007, 2009; Tembe *et al.* 2010; Moore & Lockner 2011; Kohli & Zoback 2013). The systematic evolution of the peak and steady-state friction can provide important information on the micromechanics related to strain accommodation that controls the frictional strength of the fault gouge (e.g. Saffer & Marone 2003; Behnsen & Faulkner 2012; Haines *et al.* 2013). From our experiments emerges that the applied normal stress influences the mode of strain localization while the increase of water vapour content causes a marked decrease in the absolute value of frictional strength (Fig. 4). At low normal stress (<35 MPa) friction evolves to a marked peak during the early stages of deformation, followed by a gradual strain weakening to steady-state values (Fig. 3). As the normal stress exceeds 35 MPa, sample yielding is followed by a short strain hardening stage that leads to steady-state friction (Fig. 3). This behaviour is common under different humidity conditions and initial grain size (for more details see Fig. S1). Coupling our microstructural observations with the mechanical data, we can infer the micro-mechanism governing the initial stages of fault deformation. At low normal stress, during the loading stage, the peak friction is the result of the interaction between misaligned phyllosilicate minerals with the angular-granular (quartz and calcite) grains, resulting in a high peak strength (e.g. Saffer & Marone 2003; Haines *et al.* 2009, 2013). As deformation
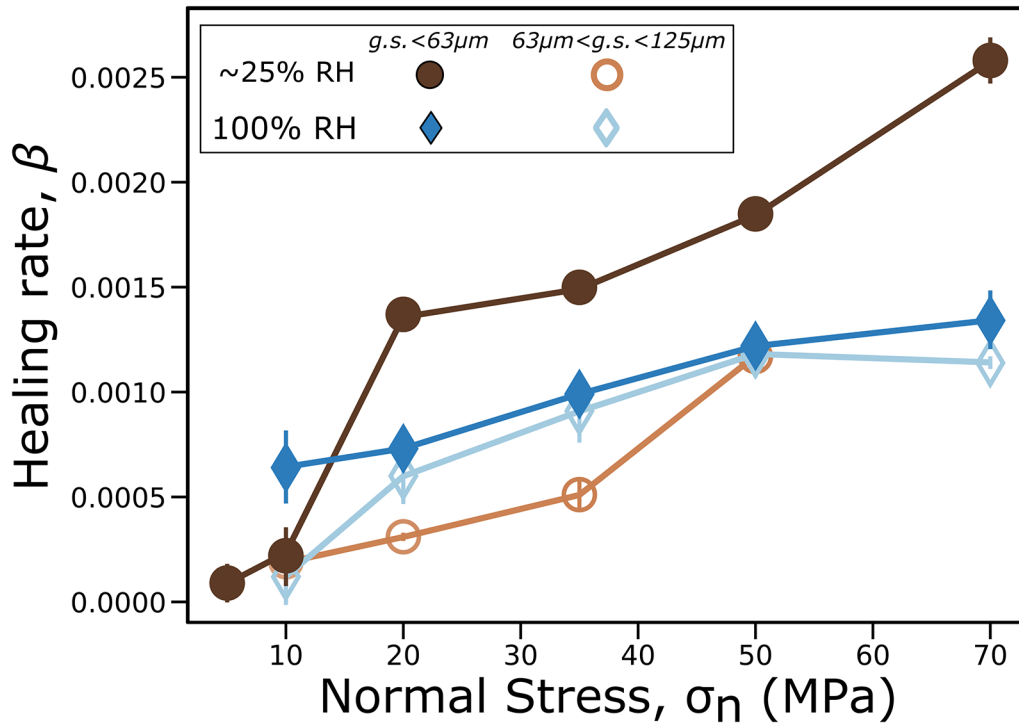
Figure 8. Evolution of Healing Rate (β) with normal stress. The data points from room humidity experiments are shown in brownish colors, whereas the 100 per cent RH ones are in blueish colors. Empty symbols (and lighter colors) are experiments at higher initial grain size ($63 < $ g.s. < 125 μm); full symbols (and darker colors) correspond to the experiments at g.s. < 63 μm. The error bars on each symbol refer to the standard deviation of the semi-log-linear fit obtained from the plots in Fig. 7.

continues after the peak friction, shear localization occurs along incipient B-shear zones (Fig. 9) causing strain weakening. This is at the origin of lower steady-state frictional strength favoured by sliding along an incipient network of phyllosilicates (e.g. Tchalenko 1970; Ikari *et al.* 2009; Morrow *et al.* 2017; Collettini *et al.* 2019). At high normal stress (>35 MPa), the absence of a peak in friction and the low frictional strength are coupled with the fabric of the experimental fault zone characterized by deformation being accommodated by R-shear (Figs 10a and c) and P-foliation (Figs 10b and d). Here, a well-developed network of phyllosilicates with S-C type fabric is in geometrical continuity with the B-shears (Figs 10e and f). This type of texture has been widely observed for a range of phyllosilicate rich fault rocks (e.g. Bos *et al.* 2000; Tembe *et al.* 2010; Haines *et al.* 2013; Morrow *et al.* 2017).

The effect of water vapour content in lowering the frictional strength of phyllosilicate-rich gouge powders has already been extensively studied (e.g. Saffer & Marone 2003; Crawford *et al.* 2008; Tembe *et al.* 2010; Moore & Lockner 2011; Behnsen & Faulkner 2012; Ruggieri *et al.* 2021). Our data clearly show that under 100 per cent RH conditions the friction coefficient is systematically lower than that from room humidity experiments ($\sim$25 per cent RH), as much as 0.1 (Fig. 4). This water-assisted weakening mechanism is typically observed in clay-rich fault gouges (e.g. Israelachvili *et al.* 1988; Saffer *et al.* 2001; Ikari *et al.* 2007; Morrow *et al.* 2017; Orellana *et al.* 2019) whereas, for pure quartz powders, the results by Frye & Marone (2002) show that increasing humidity has no effect on the steady-state coefficient of friction at a given normal stress, even if this is not always observed (e.g. Dieterich & Conrad 1984). Several processes have been invoked to explain this weakening in clay-rich fault gouges, likely related to the nature of the weak chemical bonds that hold together the platy foliae of

phyllosilicates (e.g. Bird 1984; Morrow *et al.* 2000). The increase of water vapour content can lubricate the mineral surface, weakening the chemical bonds between phyllosilicate foliae and, in turns decreasing the shear strength (Israelachvili *et al.* 1988; Morrow *et al.* 2017). We further note that the chemistry of the water can also play a crucial role in controlling frictional strength. In fact, water enriched with different solutes (calcium, salt and silica) can act as a catalyst for chemical reactions between minerals controlling the bulk mechanical response. In the context of nuclear waste disposal and carbon dioxide sequestration, the water in the repository is salty and highly charged with ions, potentially adding a further control on the frictional response of the OPA Clay. Alternatively, due to the anastomosed structure along the shear planes the water can be trapped, resulting in undetected interstitial high pore pressures that may lower the effective normal stress locally (i.e. σ_n—P_f; e.g. Saffer & Marone 2003; Faulkner *et al.* 2018; Orellana *et al.* 2018b). This phenomenon can also be related to the separation of clay particles as a swelling effect of OPA Clay (Paterson & Wong 2005). It has been widely documented the ability of OPA Clay to swell in the presence of water (e.g. Klinkenberg *et al.* 2009; Bock *et al.* 2010; Tsang *et al.* 2015; Fang *et al.* 2017; Voltolini & Ajo-Franklin 2020), giving rise to substantial increase of pore pressure, in the order of several MPa (Zhang *et al.* 2010). Taken together, the presence of water can cause changes in the mechanical behaviour of fault gouge, thus being a controlling factor for decreasing fault strength (Fang *et al.* 2017; Orellana *et al.* 2018b). From our experiments emerge that, under the same stress boundary conditions, water exerts a systematic weakening from the early shear stages (i.e. peak friction) to the steady-state of frictional sliding. Comparing the microstructures resulting from experiments under $\sim$25 per cent RH conditions with those performed under 100
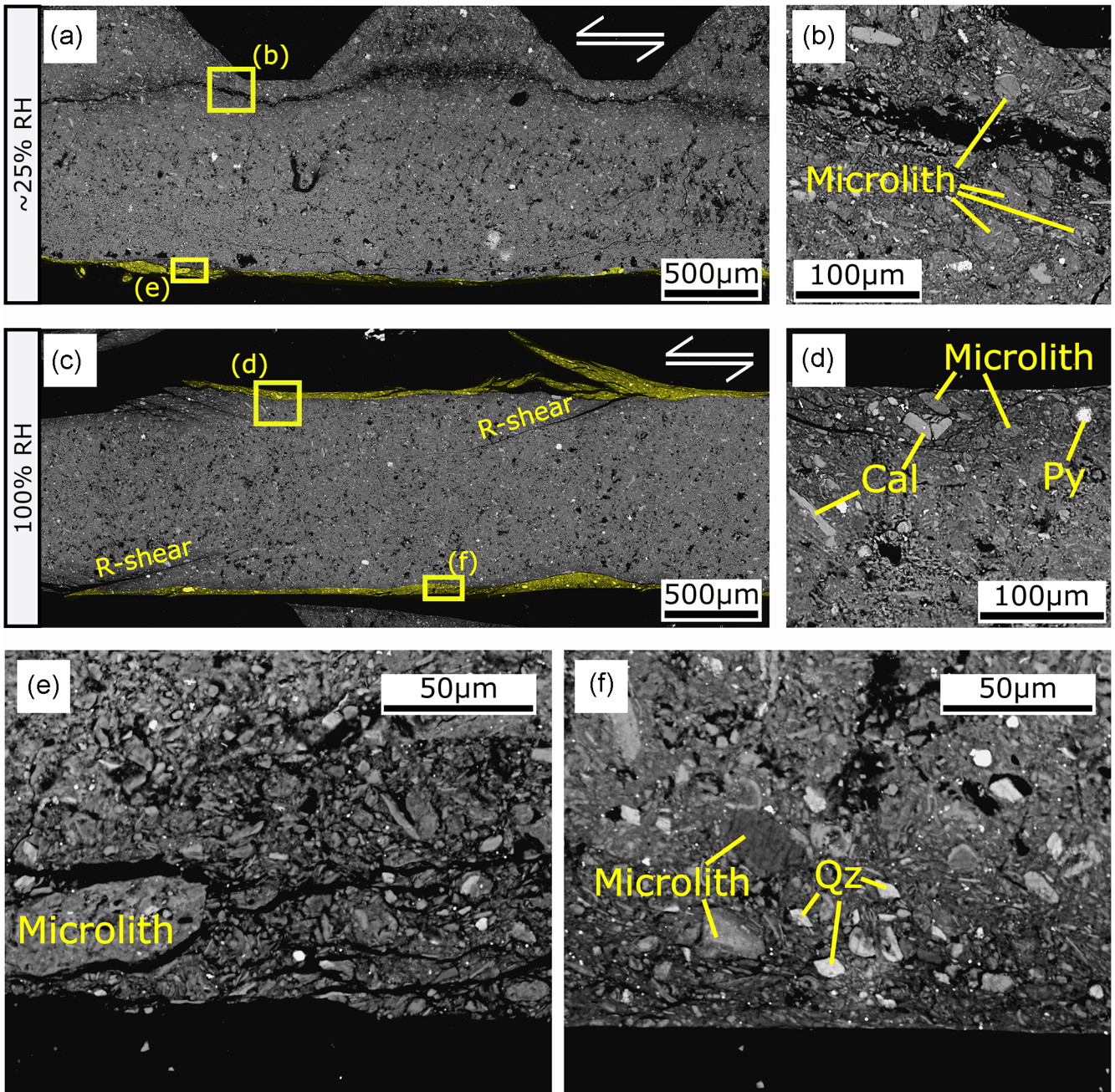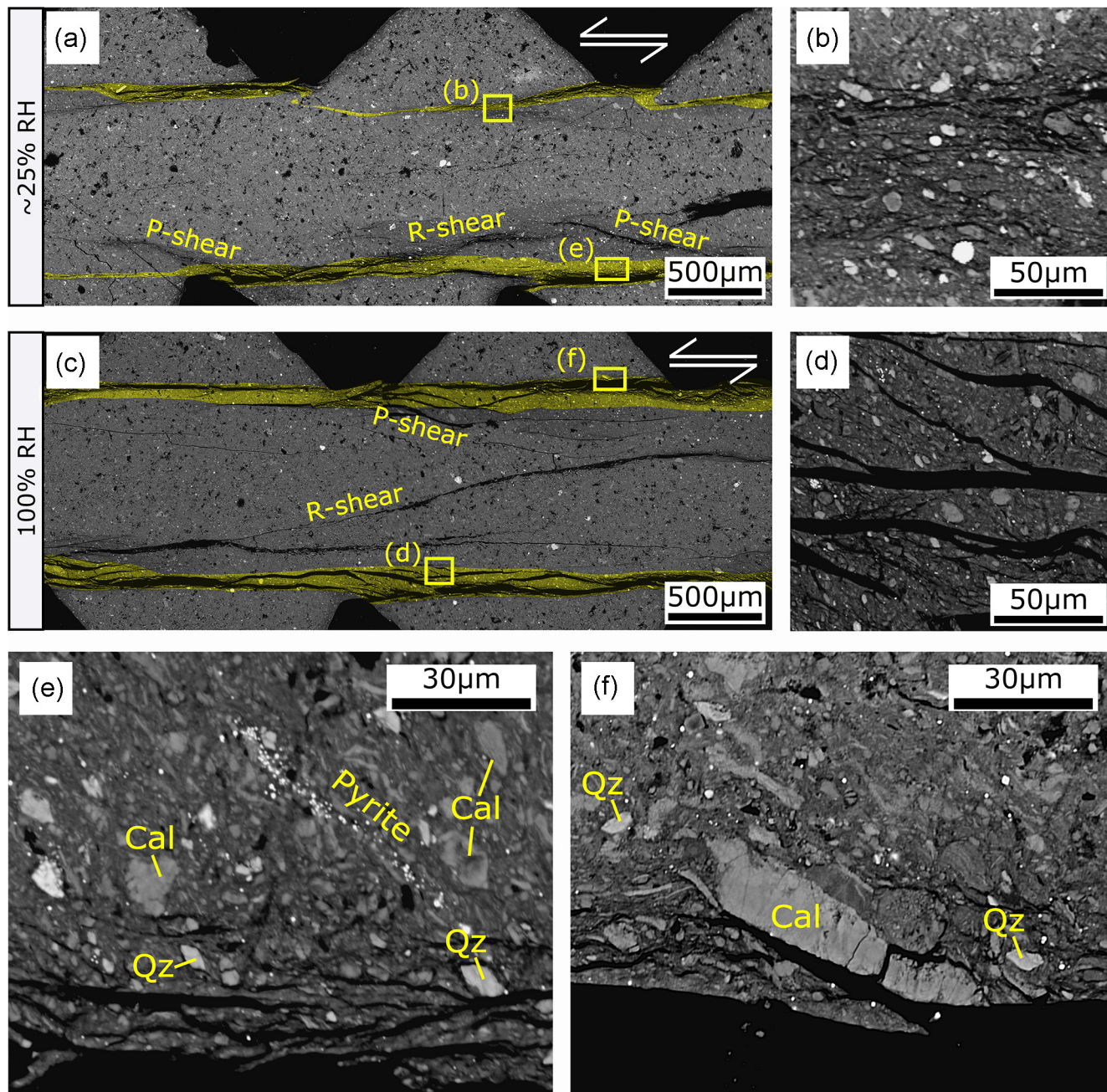
Figure 9. SEM images showing the microstructures developed in post-mortem samples, after being deformed at 10 MPa of normal stress. (a) and (c) are panoramic views of the experiments run under room humidity (∼ 25 per cent RH) and 100 per cent RH conditions, respectively. Here, the B-shears (shaded in yellow) shows different degree of shear localization, compared to the bulk deformation. In (b) and (e) are shown close-ups of the microstructures developed under room humidity conditions. (d) and (f) are the close-ups related to 100 per cent RH.

per cent RH conditions, no significant differences in strain accommodation mechanisms are observed at either low (Fig. 9) or high normal stresses (Fig. 10). The coupling of these observations highlights that frictional sliding along phyllosilicate networks is an efficient mechanism for accommodating deformation and the increase of water vapor content decreases friction without changing the style of deformation (i.e. localized or distributed) of the OPA Clay fault.

It is interesting to note that the grain size has little effect on the absolute values of peak and steady-state friction (Fig. 4, see also Fig. S1). When considering purely granular material, it has been shown that the grain size has a major effect in controlling mechanical parameters and fault stability (e.g. Marone & Kilgore 1993; Bedford & Faulkner 2021). Comparing the X-ray semiquantitative analysis of the experimental fault gouges at different grain sizes it emerges that the weight percentage of sheet silicates is similar for both grain sizes (55–58 per cent). Based on this data and microstructural observations we posit that, if the percentage of phyllosilicates is high, shear localization and frictional sliding are favoured along phyllosilicate foliae forming a continuous network (e.g. Moore & Lockner 2011), independently of initial grain size, that is at the origin of similar values of μ_{peak} and μ_{ss}.

Figure 10. SEM micrograph showing the microstructures developed in post-mortem samples, after being deformed at 70 MPa of normal stress. (a) and (c) are panoramic views of the experiments run under 25 per cent RH and 100 per cent RH conditions, respectively. Here, the B-shears (shaded in yellow) shows different degree of shear localization, compared to the bulk deformation. In (b) and (e) close-ups of the microstructures developed under room humidity conditions are shown. (d) and (f) are the close-ups related to 100 per cent RH.

4.2 The micromechanics of fault stability

The frictional stability parameter (a–b) measured for the OPA Clay always shows positive values for every initial boundary condition (i.e. humidity and grain size) and for the whole range of applied normal stress (Fig. 5, see also Fig. S5). These data therefore denote a typical velocity-strengthening behaviour that is commonly observed in mixtures of granular minerals and phyllosilicates over a critical percentage of 20–30 per cent (e.g. Niemeijer & Spiers 2006; Crawford *et al.* 2008; Tembe *et al.* 2010; Ikari *et al.* 2011; Moore & Lockner 2011; Carpenter *et al.* 2015; Giorgetti *et al.* 2015; Ruggieri *et al.* 2021) as well as in previous experiments conducted on

OPA Clay (Fang *et al.* 2017; Orellana *et al.* 2018b, 2019). From our data emerges that the parameter (a–b) mainly depends on sliding velocity and applied normal stress and subordinately on humidity conditions (Fig. 5).

At normal stress lower than 35 MPa, (a–b) strongly depends on slip velocity, which causes an increase from values close to a velocity neutral behaviour to a strong velocity strengthening as the shear velocity increases (Figs 5a and b, see also Fig. S5). This evolution of (a–b) parameter is accompanied by a positive rate dependence of fault dilation with sliding velocity (Fig. 6). At higher normal stress (>35 MPa) we observe a severe reduction of the

velocity dependence of the (*a*–*b*) parameter (Fig. 5), dilation values (Fig. 6) and critical slip distance D_c (see Fig. S6). The influence of the normal stress on the rate-dependence of (*a*–*b*) can result from the transition from localized (Fig. 9) to distributed deformation (Fig. 10) with increasing normal stress, as illuminated by microstructural analyses.

These observations have main implications for the coupling of microphysical mechanism(s) of shear accommodation with the origin of fault frictional sliding stability. The velocity dependence of the rate parameter (*a*–*b*) is commonly associated with the evolution from an asperity population, at V0, to a new population at V1, that is formed over a critical slip distance D_c (Rice & Ruina 1983; Segall & Rice 1995; Marone 1998). Our mechanical data coupled with microstructural observations suggest that above a critical normal stress of 35 MPa, there is a switch in how deformation is accommodated. We posit that when $\sigma_n < 35$ MPa, the strain is accommodated in a localized but heterogenous boundary shear zone, where larger microliths prevent the formation of a continuous foliation plane (Figs 9e and f). The preservation of some microliths testifies the lower efficiency of cataclasis due to the low normal stress, which produces the marked μ_{peak} in the initial stages (Fig. 4a). Under these conditions, upon velocity up-step, the competition between granular deformation and sliding along the phyllosilicate foliae in the heterogeneous B-shears causes the fault to dilate, promoting stabilization by the increase of (*a*–*b*) (e.g. Marone *et al.* 1990; Chen & Spiers 2016; Ikari *et al.* 2016; Chen & Niemeijer 2017). When $\sigma_n > 35$ MPa, fault gouge exhibits distributed deformation that is accommodated by wider B-shears and within the bulk volume by P-like foliation (Fig. 10). B-shear zones are also finer in grain size and display S-C fabric (Figs 10e and f). Under these boundary conditions, upon velocity perturbation, sliding is favoured along the continuous C-planes, thus decreasing the dilation of the gouge (e.g. Niemeijer & Spiers 2006; Den Hartog & Spiers 2014), which possibly explains the insensitivity of (*a*–*b*) to velocity (e.g. Saffer *et al.* 2001; Ikari *et al.* 2007).

The increase of water vapour content enhances fault stability by increasing the (*a*–*b*) parameter, both at low (Figs 5c and d) and high normal stress conditions (Figs 5e and f). By observing the dilation values (Δh) upon velocity up-steps (Fig. 6) and the microstructural texture of post-mortem samples, no significant differences between room and 100 per cent humidity conditions occur. This evidence suggests lubrication of phyllosilicate foliae can promote an increase of (*a*–*b*). Alternatively, in Section 4.2. we explored the idea of local increase of pore pressure in a well-developed phyllosilicate network, as a possible cause for lowering μ_{ss} values. After a sudden dilation upon velocity up-step the local pore pressure can be released, increasing the effective normal stress and thus, promoting frictional stability by dilatancy hardening (Segall & Rice 1995; Brantut 2020). In general, the increase of water vapour content produces the frictional strength reduction (Fig. 4) and enhances the velocity strengthening behaviour possibly inhibiting frictional instabilities (Fig. 5b; see also Ikari *et al.* 2009; Tembe *et al.* 2010; Morrow *et al.* 2017; Orellana *et al.* 2019).

As reported for the absolute values of frictional strength, the grain size does not affect the friction velocity dependence of the OPA Clay gouge, contrary to what it has been shown by previous works on granular material (e.g. Marone & Scholz 1989; Scuderi *et al.* 2017b; Bedford & Faulkner 2021). This evidence further supports the idea that, once a well-developed phyllosilicate network is formed, the frictional properties are controlled by the continuity of the fabric within the principal slip zones, regardless of the initial grain size.

From the slide-hold-slide tests we observe low values of fault healing ($0 < \Delta\mu < 0.01$, in Fig. 7) and healing rate ($0.0001 < \beta < 0.0025$, in Fig. 8) that are consistent with previous studies conducted on the OPA Clay fault gouge (Orellana *et al.* 2018b) and on phyllosilicate-rich gouges (e.g. Niemeijer & Spiers 2006; Beeler 2007; Carpenter *et al.* 2011; Tesei *et al.* 2013; Chen *et al.* 2015; Giorgetti *et al.* 2015; Okamoto *et al.* 2020). The increase of normal stress causes a progressive increase of healing and healing rate at any experimental condition. This suggests that much of the contribution to frictional healing depends on time-dependent mechanical compaction (Scholz 2019), such as interlocking of clay foliae with granular grains (Den Hartog & Spiers 2014; Orellana *et al.* 2018b).

4.3 Implication for geological repositories

In the context of geological repositories, the choice of the geological formation designated for the storage of radioactive waste, or high volumes of injected CO_2 must consider not only static physical and chemical properties of the host rock but also the mechanical behaviour of the faults occurring within the formation. Our results on the frictional strength show that a simulated fault gouge in the Opalinus clay is mechanically weak, with low friction coefficients ($\sim$0.35 to $\sim$0.41), for a wide range of normal stresses (10–70 MPa). The increase of water vapour content reduces the frictional strength under any boundary stress condition (see blue curves in Figs 11a and b). We observed that the friction curves at low normal stress are characterized by a marked μ_{peak} (Fig. 11a) that disappears at high normal stress (Fig. 11b). In the light of microstructural analysis, we observed that this disappearance corresponds to the transition from strain localization to a more distributed deformation at $\sigma_n > 35$ MPa (compare Figs 11e and f). Considering a stress gradient between 20 and 24 MPa km^{-1} at the MTL (e.g. Thury & Bossart 1999; Corkum & Martin 2007), this transition should take place at depth >1.5 km, or deeper than the operational depth of a geological repository (between 300 and 1000 m, IAEA 2012). These results could also be of importance to better constrain the eventual instability processes at the wall of galleries in the MTL. Here, during the operational and closing phases of underground galleries, the mining activities develops a so-called excavation damage zone (EDZ), where it has been long observed processes of desaturation and resaturation (Popp *et al.* 2008) which affects the efficiency of the geological barriers (Tsang *et al.* 2015). The EDZ fracture network is characterized by Mode I and Mode II fractures in the inner shell that is typically air-filled, and an outer shell which is partially water-saturated with mainly Mode I extensional fractures (Nussbaum *et al.* 2011). Under the light of our results, high relative humidity (RH) inside the underground galleries could favour the development of excavation-induced shear fractures (Mode II) by decreasing the frictional strength of OPA Clay (Fig. 11a). In addition to the effects on the near field (i.e. EDZ), a recent study by Hopp *et al.* (2022) reported small displacements ($\sim$200 µm) at slow rates (up to 1.5 nm s^{-1}), tens of meters away from the excavation site of new tunnels. The Authors located these mechanical instabilities at the boundary of the fault zone, where frictionally weak clay flakes are abundant. These findings are consistent with the localized deformation and presence of OPA Clay aggregates that we observe at normal stress <10 MPa (Fig. 11e), coupled with values of (*a*–*b*) approaching neutral at slow sliding velocities (<3 µm s^{-1}) and under $\sim$25 per cent RH conditions (Fig. 11c). Of particular importance is the mechanical behaviour upon fault reactivation (tested via velocity up-steps and SHS). Our results are in line with previous studies
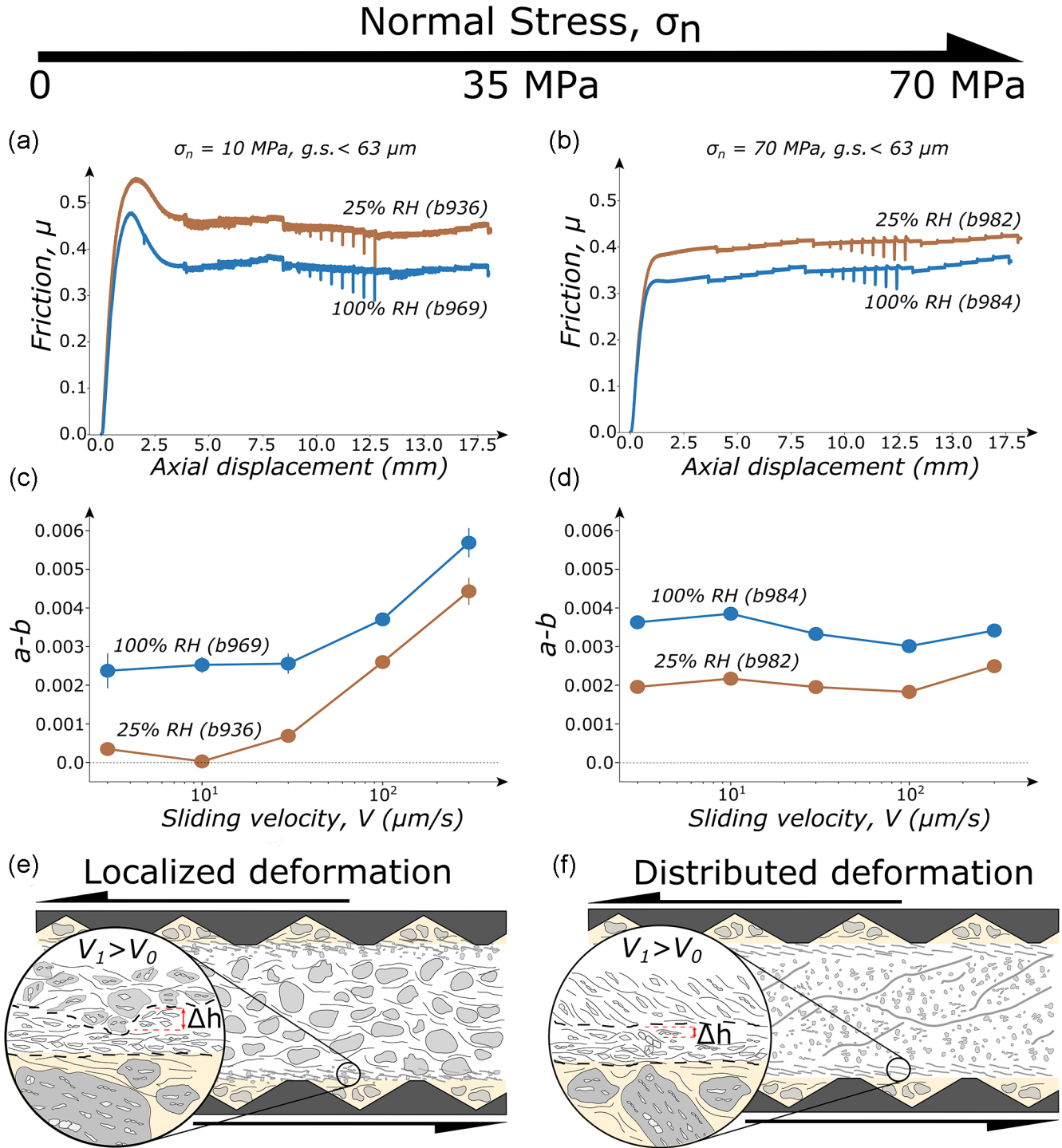
Figure 11. Conceptual model for the OPA Clay fault gouge, that summarizes the evolution of mechanical and microstructural observations as a function of normal stress. Evolution of friction with progressive axial displacement, at (a) low and (b) high normal stress. Evolution of fault stability parameter (*a–b*) at (c) low and (d) high normal stress. The increase of water vapour content decreases the friction (blue curves), increases the fault stability parameter (*a–b*) and does not affect the microstructural deformation features of the OPA Clay fault gouge. (e) Microstructural model of localized deformation under low normal stress in the B-shears, with microliths in the bulk volume. (f) Microstructural model of distributed deformation in the fault gouge under high normal stress, with a well-developed S-C type fabric and incipient P-like foliation in the B-shears. The two insets are close-ups on the micromechanical behaviour in the B-shear (dotted line) upon up-step velocity condition. At low normal stress (e), the stability is dominated by competition between granular deformation and sliding along the phyllosilicate foliae in the heterogeneous and ondulated B-shears, which promote dilation (Δ*h*). At high normal stress (f), the frictional stability is controlled by frictional sliding on well oriented phyllosilicate lamellae and dilation is reduced (see Section 4.2, for more details).

(Fang *et al.* 2017; Orellana *et al.* 2018b, 2019) that show positive values of (*a*–*b*) and low healing rate. Therefore, the experimental fault gouge in the OPA Clay is frictionally stable with few re-strengthening capabilities upon re-shear. Overall, our experimental results support the hypothesis where shear strain is accommodated by aseismic slip that may not radiate seismic energy (Orellana *et al.* 2018b). This behaviour can be compared to OPA Clay fault gouge with similar mineralogical composition and clay fabric as our samples. Further, the gouge is present as patches only in the top of the 'Main Fault', therefore the induced seismicity observed at the MTL (Guglielmi *et al.* 2020) can be attributed to structural and mineralogical heterogeneity of the fault hosted in OPA Clay. However, few key considerations should be made by considering the effect of shear velocity and normal stress. At low σ_n (<35 MPa) the stability parameter (*a*–*b*) is dependent on sliding velocity, with values that (under room humidity conditions) approach velocity neutral behaviour at 1 μm s^{-1} evolving to a strong velocity strengthening at 300 μm s^{-1} (Fig. 11c). At high σ_n (>35 MPa), while maintaining a velocity strengthening behaviour, the velocity dependence of (*a*–*b*) is severely decreased (Fig. 11d). This different evolution of (*a*–*b*) with normal stress can be important for earthquakes triggered by nearby unstable fault patches (Perfettini & Avouac 2004; Im *et al.* 2020). In the OPA Clay formation, patches of scaly clay fabric could be potentially unstable (i.e. velocity-weakening behaviour), as reported by Orellana *et al.* (2018a and 2019). Our result suggests that, at σ_n < 35 MPa, the higher rate-strengthening behaviour at higher slip velocity (Fig. 11c) may be efficient in preventing nucleation of earthquakes, quenching possible acceleration with an increase of (*a*–*b*) (Cappa *et al.* 2019). As the normal stress increases up to 70 MPa, (*a*–*b*) becomes independent of slip velocity (Fig. 11d), easing the propagation of seismic slip in weak and velocity strengthening phyllosilicate fault patches in decollement zones (e.g. Wibberley & Shimamoto 2003; Faulkner *et al.* 2011; Rowe *et al.* 2011; Bullock *et al.* 2015; Tarling *et al.* 2018). Further studies need to be done in clay-rich fault gouges to physically constrain the evolution of frictional stability parameter (*a*–*b*) with sliding velocity under a wide range of applied normal stress and pore-fluid pressures. Indeed, as observed in a recent experimental study by Jia *et al.* (2021), the increase in fluid pressure in shale samples can change the frictional stability, with potential transition from velocity strengthening to velocity weakening.

5 CONCLUSIONS

We designed frictional experiments to characterize the effect exerted by humidity, grain size and normal stress on frictional behaviour of the Opalinus clay fault gouge. We explored a wide range of normal stresses, ranging from 5 to 70 MPa performing velocity up-steps from 1 to 300 μm s^{-1} and slide-hold-slide from 1 to 3000 s.

Our experiments confirm that the OPA Clay is weak, with friction coefficients at steady-state of ~0.35 and ~0.41, for 100 per cent RH and ~25 per cent RH experiments, respectively. The OPA Clay is velocity strengthening over the entire range of applied normal stress. We observe a direct relationship between frictional parameter (*a*–*b*) and slip velocity up to 35 MPa; at higher normal stresses the (*a*–*b*) parameter seems to be velocity independent. As evidenced by the microstructural analysis, we suggest that this behaviour is due to the progressive transition with increasing normal stress, from strain localization and grain size reduction to distributed deformation on well-developed and pervasive phyllosilicate networks. The amount of relative humidity does not affect deformation mechanisms (i.e.

localized or distributed), whereas decreases fault strength and increases fault stability. We hypothesize that this is due to a possible interplay of OPA Clay swelling and lubrication, caused by the weakening of chemical bonds between phyllosilicate foliae. Notably, the initial grain size (< 63 μm or 63 < g.s. < 125 μm) does not affect either the frictional strength or stability, with similar values of dilation upon velocity up-step.

Collectively, our mechanical and microstructural observations have allowed us to build a conceptual model that summarizes the main mechanical features of the OPA Clay fault gouge. In the context of geological repositories, our results confirm that slow aseismic slip is the most likely slip behaviour for a fault gouge hosted in the OPA Clay, with similar mineralogical composition and clay fabric as our samples.

Beyond the context of deep geological repositories, this study has also implications for carbon capture and storage in the deep subsurface. Indeed, the OPA Clay shows the characteristics of a low-permeability caprock, but mechanical instabilities on the pre-existing faults can potentially generate undesired seismicity and create new hydraulic pathways that limit the sealing capacity.

DATA AVAILABILITY

The data underlying this paper are available in Zenodo, at https://doi.org/10.5281/zenodo.6685286 under the open access creative commons attribution 4.0 international license. The authors declare that they have no conflict of interest. For any other request, please contact the corresponding author at nico.bigaroni@uniroma1.it.

REFERENCES

Bedford, J. D. & Faulkner, D. R., 2021. The role of grain size and effective normal stress on localization and the frictional stability of simulated quartz gouge, *Geophys. Res. Lett.,* **48**(7).

Beeler, N. M., 2007. 13. Laboratory-observed faulting in intrinsically and apparently weak materials, in *The Seismogenic Zone of Subduction Thrust Faults,* pp. 370–449, eds Dixon, T. & Moore, C., Columbia Univ. Press.

Behnsen, J. & Faulkner, D. R., 2012. The effect of mineralogy and effective normal stress on frictional strength of sheet silicates, *J. Struct. Geol.,* **42,** 49–61.

Bhattacharya, P., Rubin, A. M. & Beeler, N. M., 2017. Does fault strengthening in laboratory rock friction experiments really depend primarily upon time and not slip?, *J. geophys. Res.,* **122**(8), 6389–6430.

Bird, P., 1984. Hydration-phase diagrams and friction of montmorillonite under laboratory and geologic conditions, with implications for shale compaction, slope stability, and strength of fault gouge, *Tectonophysics,* **107**(3-4), 235–260.

Bock, H., Dehandschutter, B., Martin, C. D., Mazurek, M., De Haller, A., Skoczylas, F. & Davy, C., 2010. *Self-Sealing of Fractures in Argillaceous Formations in the Context of Geological Disposal of Radioactive Waste,* OECD Publishing.

Bos, B., Peach, C. J. & Spiers, C. J., 2000. Frictional-viscous flow of simulated fault gouge caused by the combined effects of phyllosilicates and pressure solution, *Tectonophysics,* **327**(3-4), 173–194.

Bossart, P. *et al.*, 2018. Mont Terri rock laboratory, 20 years of research: introduction, site characteristics and overview of experiments, *Swiss J. Geosci.,* **110**, 3–22.

Brantut, N., 2020. Dilatancy-induced fluid pressure drop during dynamic rupture: direct experimental evidence and consequences for earthquake dynamics, *Earth planet. Sci. Lett.,* **538**, doi:10.1016/j.epsl.2020.116179.

Bullock, R. J., De Paola, N. & Holdsworth, R. E., 2015. An experimental investigation into the role of phyllosilicate content on earthquake propagation during seismic slip in carbonate faults, *J. geophys. Res.,* **120**(5), 3187–3207.

Byerlee, J., 1978. Friction of rocks, in *Rock Friction and Earthquake Prediction,* pp. 615–626, Birkhäuser.

Cappa, F., Guglielmi, Y. & De Barros, L., 2022. Transient evolution of permeability and friction in a slowly slipping fault activated by fluid pressurization, *Nat. Commun.,* **13**(1), doi:10.1038/s41467-022-30798-3.

Cappa, F., Scuderi, M. M., Collettini, C., Guglielmi, Y. & Avouac, J. P., 2019. Stabilization of fault slip by fluid injection in the laboratory and in situ, *Sci. Adv.,* **5**(3), doi:10.1126/sciadv.aau4065.

Carpenter, B. M., Marone, C. & Saffer, D. M., 2011. Weakness of the San Andreas Fault revealed by samples from the active fault zone, *Nat. Geosci.,* **4**(4), 251–254.

Carpenter, B. M., Saffer, D. M. & Marone, C., 2015. Frictional properties of the active San Andreas Fault at SAFOD: implications for fault strength and slip behaviour, *J. geophys. Res.,* **120**(7), 5273–5289.

Chen, J. & Niemeijer, A. R., 2017. Seismogenic potential of a gouge-filled fault and the criterion for its slip stability: constraints from a microphysical model, *J. geophys. Res.,* **122**(12), 9658–9688.

Chen, J. & Spiers, C. J., 2016. Rate and state frictional and healing behaviour of carbonate fault gouge explained using microphysical model, *J. geophys. Res.,* **121**(12), 8642–8665.

Chen, J., Verberne, B. A. & Spiers, C. J., 2015. Interseismic re-strengthening and stabilization of carbonate faults by "non-Dieterich" healing under hydrothermal conditions, *Earth planet. Sci. Lett.,* **423**, 1–12.

Collettini, C. *et al.*, 2014. A novel and versatile apparatus for brittle rock deformation, *Int. J. Rock Mech. Min. Sci.,* **66**, 114–123.

Collettini, C., Tesei, T., Scuderi, M. M., Carpenter, B. M. & Viti, C., 2019. Beyond Byerlee friction, weak faults and implications for slip behavior, *Earth planet. Sci. Lett.,* **519**, 245–263.

Corkum, A. G. & Martin, C. D., 2007. Modelling a mine-by test at the Mont Terri rock laboratory, Switzerland, *Int. J. Rock Mech. Min. Sci.,* **44**(6), 846–859.

Crawford, B. R., Faulkner, D. R. & Rutter, E. H., 2008. Strength, porosity, and permeability development during hydrostatic and shear loading of synthetic quartz-clay fault gouge, *J. geophys. Res.,* **113**(B3), doi:10.1029/2006JB004634.

Den Hartog, S. A. & Spiers, C. J., 2013. Influence of subduction zone conditions and gouge composition on frictional slip stability of megathrust faults, *Tectonophysics,* **600**, 75–90.

Den Hartog, S. A. & Spiers, C. J., 2014. A microphysical model for fault gouge friction applied to subduction megathrusts, *J. geophys. Res.,* **119**(2), 1510–1529.

Dieterich, J. H., 1979. Modeling of rock friction: 1. Experimental results and constitutive equations, *J. geophys. Res.,* **84**(B5), 2161–2168.

Dieterich, J. H. & Conrad, G., 1984. Effect of humidity on time-and velocity-dependent friction in rocks, *J. geophys. Res.,* **89**(B6), 4196–4202.

Fang, Y., Elsworth, D., Wang, C., Ishibashi, T. & Fitts, J. P., 2017. Frictional stability-permeability relationships for fractures in shales, *J. geophys. Res.,* **122**(3), 1760–1776.

Fang, Y., Elsworth, D., Wang, C. & Jia, Y., 2018. Mineralogical controls on frictional strength, stability, and shear permeability evolution of fractures, *J. geophys. Res.,* **123**(5), 3549–3563.

Faulkner, D. R., Mitchell, T. M., Behnsen, J., Hirose, T. & Shimamoto, T., 2011. Stuck in the mud? Earthquake nucleation and propagation through accretionary forearcs, *Geophys. Res. Lett.,* **38**(18), doi:10.1029/2011GL048552.

Faulkner, D. R., Sanchez-Roa, C., Boulton, C. & Den Hartog, S. A. M., 2018. Pore fluid pressure development in compacting fault gouge in theory, experiments, and nature, *J. geophys. Res.,* **123**(1), 226–241.

Frye, K. M. & Marone, C., 2002. Effect of humidity on granular friction at room temperature, *J. geophys. Res.,* **107**(B11), ETG 11–1-ETG 11-13.

Giacomel, P., Ruggieri, R., Scuderi, M. M., Spagnuolo, E., Di Toro, G. & Collettini, C., 2021. Frictional properties of basalt experimental faults and implications for volcano-tectonic settings and geo-energy sites, *Tectonophysics,* **811**, doi:10.1016/j.tecto.2021.228883.

Giorgetti, C., Carpenter, B. M. & Collettini, C., 2015. Frictional behaviour of talc-calcite mixtures, *J. geophys. Res.,* **120**(9), 6614–6633.

Guglielmi, Y., Nussbaum, C., Jeanne, P., Rutqvist, J., Cappa, F. & Birkholzer, J., 2020. Complexity of fault rupture and fluid leakage in shale: insights from a controlled fault activation experiment, *J. geophys. Res.,* **125**(2), e2019JB017781, doi:10.1029/2019JB017781.

Haines, S. H., Kaproth, B., Marone, C., Saffer, D. & Van der Pluijm, B., 2013. Shear zones in clay-rich fault gouge: a laboratory study of fabric development and evolution, *J. Struct. Geol.,* **51**, 206–225.

Haines, S. H., Van Der Pluijm, B. A., Ikari, M. J., Saffer, D. M. & Marone, C., 2009. Clay fabric intensity in natural and artificial fault gouges: implications for brittle fault zone processes and sedimentary basin clay fabric evolution, *J. geophys. Res.,* **114**(B5), doi:10.1029/2008JB005866.

Hopp, C. *et al.*, 2022. The effect of fault architecture on slip behavior in shale revealed by distributed fiber optic strain sensing, *J. geophys. Res.,* **127**(1), e2021JB022432, doi:10.1029/2021JB022432.

IAEA., 2012. The safety case and safety assessment for the disposal of radioactive waste, IAEA Safety Standards Series, Specific Safety Guide No. SSG-23, STI/PUB/1553, IAEA, Vienna, Austria.

Ikari, M. J., Carpenter, B. M. & Marone, C., 2016. A microphysical interpretation of rate-and state-dependent friction for fault gouge, *Geochem. Geophys. Geosyst.,* **17**(5), 1660–1677.

Ikari, M. J., Marone, C. & Saffer, D. M., 2011. On the relation between fault strength and frictional stability, *Geology,* **39**(1), 83–86.

Ikari, M. J., Saffer, D. M. & Marone, C., 2007. Effect of hydration state on the frictional properties of montmorillonite-based fault gouge, *J. geophys. Res.,* **112**(B6), doi:10.1029/2006JB004748.

Ikari, M. J., Saffer, D. M. & Marone, C., 2009. Frictional and hydrologic properties of clay-rich fault gouge, *J. geophys. Res.,* **114**(B5), doi:10.1029/2008JB006089.

Im, K., Elsworth, D. & Fang, Y., 2018. The influence of preslip sealing on the permeability evolution of fractures and faults, *Geophys. Res. Lett.,* **45**(1), 166–175.

Im, K., Saffer, D., Marone, C. & Avouac, J. P., 2020. Slip-rate-dependent friction as a universal mechanism for slow slip events, *Nat. Geosci.,* **13**(10), 705–710.

Israelachvili, J. N., McGuiggan, P. M. & Homola, A. M., 1988. Dynamic properties of molecularly thin liquid films, *Science,* **240**(4849), 189–191.

Jeanne, P., Guglielmi, Y., Rutqvist, J., Nussbaum, C. & Birkholzer, J., 2018. Permeability variations associated with fault reactivation in a claystone formation investigated by field experiments and numerical simulations, *J. geophys. Res.,* **123**(2), 1694–1710.

Jia, Y., Tang, J., Lu, Y. & Lu, Z., 2021. The effect of fluid pressure on frictional stability transition from velocity strengthening to velocity weakening and critical slip distance evolution in shale reservoirs, *Geomech. Geophys. Geo-Ener. Geo-Resour.,* **7**(1), 1–13.

Klinkenberg, M., Kaufhold, S., Dohrmann, R. & Siegesmund, S., 2009. Influence of carbonate microfabrics on the failure strength of claystones, *Eng. Geol.,* **107**(1-2), 42–54.

Kohli, A. H. & Zoback, M. D., 2013. Frictional properties of shale reservoir rocks, *J. geophys. Res.,* **118**(9), 5109–5125.

Laurich, B., Urai, J. L. & Nussbaum, C., 2017. Microstructures and deformation mechanisms in Opalinus Clay: insights from scaly clay from the Main Fault in the Mont Terri Rock Laboratory (CH), *Solid Earth,* **8**(1), 27–44.

Laurich, B., Urai, J. L., Vollmer, C. & Nussbaum, C., 2018. Deformation mechanisms and evolution of the microstructure of gouge in the Main Fault in Opalinus Clay in the Mont Terri rock laboratory (CH), *Solid Earth,* **9**(1), 1–24.

Logan, J. M., Dengo, C. A., Higgs, N. G. & Wang, Z. Z., 1992. Fabrics of experimental fault zones: their development and relationship to mechanical behaviour, in *International Geophysics,* Vol. **51**, pp. 33–67, Academic Press.

Mair, K. & Marone, C., 1999. Friction of simulated fault gouge for a wide range of velocities and normal stresses, *J. geophys. Res.,* **104**(B12), 28 899–28 914.

Marone, C., 1998. Laboratory-derived friction laws and their application to seismic faulting, *Annu. Rev. Earth planet. Sci.,* **26**(1), 643–696.

Marone, C., Hobbs, B. E. & Ord, A., 1992. Coulomb constitutive laws for friction: contrasts in frictional behaviour for distributed and localized shear, *Pure appl. Geophys.,* **139**(2), 195–214.

Marone, C. & Kilgore, B., 1993. Scaling of the critical slip distance for seismic faulting with shear strain in fault zones, *Nature,* **362**(6421), 618–621.

Marone, C., Raleigh, C. B. & Scholz, C. H., 1990. Frictional behaviour and constitutive modeling of simulated fault gouge, *J. geophys. Res.,* **95**(B5), 7007–7025.

Marone, C. & Scholz, C. H., 1989. Particle-size distribution and microstructures within simulated fault gouge, *J. Struct. Geol.,* **11**(7), 799–814.

Moore, D. E. & Lockner, D. A., 2011. Frictional strengths of talc-serpentine and talc-quartz mixtures, *J. geophys. Res.,* **116**(B1), doi:10.1029/2010JB 007881.

Moore, D. M. & Reynolds, R. C., 1997. *X-Ray Diffraction and the Identification and Analysis of Clay Minerals,* Oxford Univ. Press.

Morrow, C. A., Moore, D. E. & Lockner, D. A., 2000. The effect of mineral bond strength and adsorbed water on fault gouge frictional strength, *Geophys. Res. Lett.,* **27**(6), 815–818.

Morrow, C. A., Moore, D. E. & Lockner, D. A., 2017. Frictional strength of wet and dry montmorillonite, *J. geophys. Re.,* **122**(5), 3392–3409.

Niemeijer, A. R. & Spiers, C. J., 2006. Velocity dependence of strength and healing behaviour in simulated phyllosilicate-bearing fault gouge, *Tectonophysics,* **427**(1-4), 231–253.

Nussbaum, C., Bossart, P., Amann, F. & Aubourg, C., 2011. Analysis of tectonic structures and excavation induced fractures in the Opalinus Clay, Mont Terri underground rock laboratory (Switzerland), *Swiss J. Geosci.,* **104**(2), 187–210.

Nussbaum, C., Kloppenburg, A., Caër, T. & Bossart, P., 2018. Tectonic evolution around the Mont Terri rock laboratory, northwestern Swiss Jura: constraints from kinematic forward modelling, in *Mont Terri Rock Laboratory, 20 Years,* pp. 41–68, Birkhäuser.

Okamoto, A. S., Niemeijer, A. R., Takeshita, T., Verberne, B. A. & Spiers, C. J., 2020. Frictional properties of actinolite-chlorite gouge at hydrothermal conditions, *Tectonophysics,* **779**, 228377.

Orellana, L. F., Giorgetti, C. & Violay, M., 2019. Contrasting mechanical and hydraulic properties of wet and dry fault zones in a proposed shale-hosted nuclear waste repository, *Geophys. Res. Lett.,* **46**(3), 1357–1366.

Orellana, L. F., Scuderi, M. M., Collettini, C. & Violay, M., 2018a. Do scaly clays control seismicity on faulted shale rocks?, *Earth planet. Sci. Lett.,* **488**, 59–67.

Orellana, L. F., Scuderi, M. M., Collettini, C. & Violay, M., 2018b. Frictional properties of Opalinus Clay: implications for nuclear waste storage, *J. geophys. Res.,* **123**(1), 157–175.

Passchier, C. W. & Trouw, R. A., 2005. *Microtectonics,* Springer Science & Business Media.

Paterson, M. S. & Wong, T. F., 2005. *Experimental Rock Deformation—The Brittle Field,* Springer Science & Business Media.

Perfettini, H. & Avouac, J. P., 2004. Postseismic relaxation driven by brittle creep: a possible mechanism to reconcile geodetic measurements and the decay rate of aftershocks, application to the Chi-Chi earthquake, Taiwan, *J. geophys. Res.,* **109**(B2), doi:10.1029/2003JB002488.

Popp, T., Salzer, K. & Minkley, W., 2008. Influence of bedding planes to EDZ-evolution and the coupled HM properties of Opalinus Clay, *Phys. Chem. Earth, Parts A/B/C,* **33**, S374–S387.

Reinen, L. A. & Weeks, J. D., 1993. Determination of rock friction constitutive parameters using an iterative least squares inversion method, *J. Geophys. Res.: Solid Earth,* **98**(B9), 15937–15950.

Rice, J.R. & Ruina, A.L., 1983. Stability of steady frictional slipping, *J. Appl. Mech.,* **105**, 343–349.

Rowe, C. D., Meneghini, F. & Moore, J. C., 2011. Textural record of the seismic cycle: strain-rate variation in an ancient subduction thrust, *Geol. Soc., Lond., Spec. Publ.,* **359**(1), 77–95.

Ruggieri, R. *et al.*, 2021. The role of shale content and pore-water saturation on frictional properties of simulated carbonate faults, *Tectonophysics,* **807**, 228811.

Ruina, A., 1983. Slip instability and state variable friction laws, *J. geophys. Res.,* **88**(B12), 10 359–10 370.

Rutqvist, J., Rinaldi, A. P., Cappa, F., Jeanne, P., Mazzoldi, A., Urpi, L., Guglielmi, Y. & Vilarrasa, V., 2016. Fault activation and induced seismicity in geological carbon storage–lessons learned from recent modeling studies, *J. Rock Mech. Geotech. Eng.,* **8**(6), 789–804.

Saffer, D. M., Frye, K. M., Marone, C. & Mair, K., 2001. Laboratory results indicating complex and potentially unstable frictional behaviour of smectite clay, *Geophys. Res. Lett.,* **28**(12), 2297–2300.

Saffer, D. M. & Marone, C., 2003. Comparison of smectite-and illite-rich gouge frictional properties: application to the updip limit of the seismogenic zone along subduction megathrusts, *Earth planet. Sci. Lett.,* **215**(1-2), 219–235.

Samuelson, J., Elsworth, D. & Marone, C., 2009. Shear-induced dilatancy of fluid-saturated faults: experiment and theory, *J. geophys. Res.,* **114**(B12), doi:10.1029/2008JB006273.

Samuelson, J. & Spiers, C. J., 2012. Fault friction and slip stability not affected by CO_2 storage: evidence from short-term laboratory experiments on North Sea reservoir sandstones and caprocks, *Int. J. Greenhouse Gas Contl.,* **11**, S78–S90.

Scholz, C. H., 1998. Earthquakes and friction laws, *Nature,* **391**(6662), 37–42.

Scholz, C. H., 2019. *The Mechanics of Earthquakes and Faulting.* Cambridge Univ. Press.

Scott, D. R., Marone, C. J. & Sammis, C. G., 1994. The apparent friction of granular fault gouge in sheared layers, *J. geophys. Res.,* **99**(B4), 7231–7246.

Scuderi, M. M. & Collettini, C., 2018. Fluid injection and the mechanics of frictional stability of shale-bearing faults, *J. geophys. Res.,* **123**(10), 8364–8384.

Scuderi, M. M., Collettini, C. & Marone, C., 2017a. Frictional stability and earthquake triggering during fluid pressure stimulation of an experimental fault, *Earth planet. Sci. Lett.,* **477**, 84–96.

Scuderi, M. M., Collettini, C., Viti, C., Tinti, E. & Marone, C., 2017b. Evolution of shear fabric in granular fault gouge from stable sliding to stick slip and implications for fault slip mode, *Geology,* **45**(8), 731–734.

Segall, P. & Rice, J. R., 1995. Dilatancy, compaction, and slip instability of a fluid-infiltrated fault, *J. geophys. Res.,* **100**(B11), 22 155–22 171.

Segall, P., Rubin, A. M., Bradley, A. M. & Rice, J. R., 2010. Dilatant strengthening as a mechanism for slow slip events, *J. geophys. Res.,* **115**(B12), doi:10.1029/2010JB007449.

Tarling, M. S., Smith, S. A., Viti, C. & Scott, J. M., 2018. Dynamic earthquake rupture preserved in a creeping serpentinite shear zone, *Nat. Commun.,* **9**(1), 1–8.

Tchalenko, J. S., 1970. Similarities between shear zones of different magnitudes, *Bull. geol. Soc. Am.,* **81**(6), 1625–1640.

Tembe, S., Lockner, D. A. & Wong, T. F., 2010. Effect of clay content and mineralogy on frictional sliding behaviour of simulated gouges: binary and ternary mixtures of quartz, illite, and montmorillonite, *J. geophys. Res.,* **115**(B3), doi:10.1029/2009JB006383.

Tesei, T., Collettini, C., Viti, C. & Barchi, M. R., 2013. Fault architecture and deformation mechanisms in exhumed analogues of seismogenic carbonate-bearing thrusts, *J. Struct. Geol.,* **55,** 167–181.

Thury, M. & Bossart, P., 1999. The Mont Terri rock laboratory, a new international research project in a Mesozoic shale formation, in Switzerland, *Eng. Geol.,* **52**(3-4), 347–359.

Tsang, C. F., Barnichon, J. D., Birkholzer, J., Li, X. L., Liu, H. H. & Sillen, X., 2012. Coupled thermo-hydro-mechanical processes in the near field of a high-level radioactive waste repository in clay formations, *Int. J. Rock Mech. Min. Sci.,* **49,** 31–44.

Tsang, C. F., Neretnieks, I. & Tsang, Y., 2015. Hydrologic issues associated with nuclear waste repositories, *Water Resour. Res.,* **51**(9), 6923–6972.

Voltolini, M. & Ajo-Franklin, J. B., 2020. The sealing mechanisms of a fracture in opalinus clay as revealed by in situ synchrotron x-ray microtomography, *Front. Earth Sci.,* **8,** 207.

Walsh, F. R. & Zoback, M. D., 2016. Probabilistic assessment of potential fault slip related to injection-induced earthquakes: application to north-central Oklahoma, USA, *Geology,* **44**(12), 991–994.

Wang, W. L., Wang, T. T., Su, J. J., Lin, C. H., Seng, C. R. & Huang, T. H., 2001. Assessment of damage in mountain tunnels due to the Taiwan Chi-Chi earthquake, *Tunnell. Underground Space Technol.,* **16**(3), 133–150.

Wibberley, C. A. & Shimamoto, T., 2003. Internal structure and permeability of major strike-slip fault zones: the median tectonic line in mie prefecture, Southwest Japan, *J. Struct. Geol.,* **25**(1), 59–78.

Zappone, A. *et al.*, 2021. Fault sealing and caprock integrity for CO_2 storage: an in situ injection experiment, *Solid Earth,* **12**(2), 319–343.

Zhang, C. L., Wieczorek, K. & Xie, M. L., 2010. Swelling experiments on mudstones, *J. Rock Mech. Geotech. Eng.,* **2**(1), 44–51.

Zhang, S. & Cox, S. F., 2000. Enhancement of fluid permeability during shear deformation of a synthetic mud, *J. Struct. Geol.,* **22**(10), 1385–1393.

SUPPORTING INFORMATION

Supplementary data are available at *GJI* online.

Table S1. Experimental boundary conditions, frictional strength and parameters.
Figure S1. Frictional evolution curves for all the experiments.
Figure S2. Evolution of the layer thickness during shear sliding.
Figure S3. Calculation of the dilatancy coefficient.
Figure S4. Microstructural analysis of 5 post-mortem specimens.
Figure S5. Details of velocity dependence of RSF parameters.
Figure S6. Evolution of critical slip distance (Dc) with normal stress and humidity.

Please note: Oxford University Press is not responsible for the content or functionality of any supporting materials supplied by the authors. Any queries (other than missing material) should be directed to the corresponding author for the paper.